Dynamical Prototype of the Arctic Oscillation as Revealed by a Neutral Singular Vector

Masahiro Watanabe[1] and Fei-fei Jin[2]

1: Division of Ocean and Atmospheric Science, Hokkaido University
Nishi 5, Kita 10, Sapporo, Hokkaido 060–0810, Japan

2: Department of Meteorology, University of Hawaii at Manoa
2525 Correa Road, Honolulu, HI 96822, USA

submitted to the *Journal of Climate*

July 18, 2003

* Corresponding author: Dr. M. Watanabe, E–mail: hiro@ees.hokudai.ac.jp

ABSTRACT

Origin of the Arctic Oscillation (AO) was explored from dynamical perspective, using a primitive equation model linearized about the observed winter climatology. In order to obtain a leading low–frequency mode of the model atmosphere, singular vector analysis is performed to the linear dynamical operator. The singular mode (v–vector) with the smallest singular value, referred to as the neutral mode, has a considerable similarity to the observed AO in many aspects, suggesting that, at least in a linear dynamical framework, the AO is a dynamically consistent mode of variability that arises from the zonal asymmetry of the time mean state.

Diagnosis of the neutral mode shows that a zonal flow–stationary wave interaction and an interaction between anomalous and climatological stationary waves are both of importance for maintenance of the spatial structure. Besides the vortex stretching/shrinking is significant in the upper level, which manifests that a baroclinic process has a certain role as well. It is found that the formation of a hemispheric scale of the neutral mode is accomplished within several days via propagation of Rossby wave packets along the jetstreams which act as waveguide. The neutral mode structure is robust for a wide range of model damping parameters, and especially preferred when the damping is weakened in the free troposphere. The corresponding optimal forcing (u–vector) indicates that, though its robustness is relatively ambiguous, the neutral mode is the most effectively excited by a certain pattern of the extratropical thermal forcing, in addition to a modest sensitivity to the deep heating anomaly over the tropical Indian Ocean.

1 Introduction

A concept of Arctic Oscillation (AO), or the northern annular mode, proposed by Thompson and Wallace (1998) has recently provided a different view of the low–frequency atmospheric variability from the classic teleconnection. The AO, defined by the leading empirical orthogonal function (EOF) to the Northern Hemisphere sea level pressure (SLP) anomalies, has a hemispheric extent dominated by a zonally uniform structure as shown by the AO–covariant height anomalies (Fig. 1a). Insofar, there is a stimulated discussion on several aspects associated with AO: for example, coupling between the troposphere and the stratosphere (e.g. Kodera and Kuroda 1999; Baldwin and Dunkerton 1999), impacts on regional climate (Thompson and Wallace 2001), and the similarity to a linear trend in the observed atmosphere or the future prediction in global warming simulations (Shindell et al. 1999; Fyfe et al. 1999, among others).

On the other hand, the introduction of the AO concept also results in a confusion to the pre–existed North Atlantic Oscillation (NAO) paradigm (Hurrell 1995). Since the AO pattern is almost the same as the NAO except for the Pacific center of action, which is absent in the latter, and indices for both phenomena are nearly perfectly correlated, the AO and NAO are hardly distinguished by their time sequences. For this reason, there is an extensive debate on which mode of variability, i.e. between the AO and NAO, is more physically relevant (Wallace 2000). The key component in question is the Pacific center of action in the AO; Deser (2000), Ambaum et al. (2001), and Itoh (2002) all emphasize the lack of statistical covariability between the Pacific and Atlantic SLP anomalies associated with the AO, leading to a conclusion that the AO is apparent but not a physically meaningful mode. Wallace and Thompson (2002) counteract this argument and suggest that the absence of significant correlations between the SLP anomalies over the two ocean basins comes from a contamination by another dominant variability that is anti–symmetric over the North Pacific and the North Atlantic (Honda and Nakamura 2001).

The above studies examine the AO/NAO paradigm based on statistical analyses of the

observed fields, which may have a limit to delineate the dynamical relevance of the AO. This study attempts to join this issue from the dynamical perspective, namely, by exploring whether the origin of AO resides in the time–mean state of the atmospheric.

A well–known fact is that both the AO and NAO accompany a meridional dipole in zonal–mean zonal wind anomalies, which shows the westerly (easterly) anomaly around 60°N (30°N) in its positive phase (Fig. 1b). It has been pointed out that the zonal wind dipole is formed mainly by the momentum forcing due to anomalous stationary waves of the AO/NAO (Limpasuvan and Hartmann 1999; DeWeaver and Nigam 2000a). Subsequently, DeWeaver and Nigam (2000b), who carefully used a linearized primitive equation model, showed that the stationary wave anomaly associated with the NAO can be in turn excited by the zonal flow anomaly of the NAO itself, strongly suggesting a positive wave–zonal flow feedback at work for the AO/NAO. Natural extension of these studies is made by Kimoto et al. (2001), who used a linear model similar to that of DeWeaver and Nigam (2000b) but computed the so–called singular modes of the zonal mean state in which the stationary wave feedback has been parameterized. Although the parameterization ignores an interaction between stationary waves, the mode that dominates in the quasi–stationary fields considerably resembles the observed AO in terms of the zonal wind dipole and associated stationary wave anomalies.

Theory of the singular mode, which is somewhat different from the conventional normal mode theory, is first proposed by Dymnikov (1988) and Navarra (1993) for the meteorological fields. A near–neutral singular mode is equivalent to the dynamical mode that has the largest amplitude in a steady atmospheric response forced by spatially random noise (Branstator 1990, see section 2c). Similar to a barotropic instability mode (Simmons et al. 1983), such a mode gains energy from the zonal inhomogeniety of the basic state, therefore stationary waves in the time–mean state are crucially important for determining the structure of the neutral singular mode. While the relevance of the neutral singular mode in the atmospheric low–frequency variability is examined by several studies (Marshall and Molteni 1993; Itoh and Kimoto 1999),

those are carried out with a relatively simple dynamical basis such as the two–to–three level quasi–geostrophic models, or further simpler barotropic model in many cases (e.g. Navarra 1993; Metz 1994; Bladé 1996). Kimoto et al. (2001) adopted a 20–level primitive equation model, but the singular mode of the fully 3D atmosphere is not calculated.

The present study is to extend our earlier work, Kimoto et al. (2001), with the aim at obtaining a complete set of dynamical modes in the extratropical atmosphere. This attempt will not only improve the previous computation, but also add some insights into the 3D structure of an effective forcing to the preferred low–frequency variability of the atmosphere. We also perform several diagnoses to delineate how and why the neutral mode structure, which shares common features with the observed AO, is favored by the 3D time–mean state of the atmosphere.

This paper is organized as follows. Section 2 describes observational data, the linear atmospheric model used in this study, and reviews a theoretical basis of the singular modes. In section 3, structure of the neutral singular vector is first shown, followed by analyses of the dynamical balance, temporal evolution, and sensitivity to dissipation parameters. Section 4 presents a forcing associated with the neutral singular vector, in order to obtain clues to a question whether we can specify an external forcing pattern which is optimal in exciting the AO/NAO. The results of the singular mode analysis are summarized and the implication is discussed in sections 5.

2 Data, model and theory

a. Observational data

Observed atmospheric fields used in this study are derived from the NCEP/NCAR reanalysis (Kalnay et al. 1996) which spans from January 1948 to December 2002. The data are available on a 2.5°× 2.5°grid at standard pressure levels. For each variable the monthly climatology

was first subtracted and then averaged during winter (December, January, and February). The winter anomalies are regressed onto the winter AO index[1] as conventionally defined by the principal component associated with the leading EOF of the monthly 1000 hPa height (equivalent to SLP) anomaly (Thompson and Wallace 1998, 2000). Regressed anomalies corresponding to one standard deviation of the AO index are hereafter referred to as the AO anomaly. Example of the AO anomaly is presented in Fig. 1. The anomalous geopotential height at 300 hPa (Fig. 1a) reveals a zonally oriented pattern as noted, which accompanies a north–south dipole in the zonal–mean zonal wind anomalies (Fig. 1b). Eliassen–Palm (E–P) fluxes associated with the AO stationary wave anomaly is evident in forcing the zonal wind dipole (arrows in Fig. 1b). All of these anomalies characterize the basic feature of the AO.

b. Linear baroclinic model

The atmospheric model is based on a linear primitive equations, usually called the linear baroclinic model (LBM). Suppose a state vector $\boldsymbol{X}$, which consists of vorticity (ζ), divergence (D), temperature (T) and logarithm of surface pressure (Ps), satisfies nonlinear primitive equations with external forcing. When we consider small perturbations as defined by the deviation from a basic state $\boldsymbol{X}_c$, i.e.,

$$\boldsymbol{X}_a = \boldsymbol{X} - \boldsymbol{X}_c \quad ,$$

a linear dynamical operator of the LBM, denoted as $\boldsymbol{L}$, may be computed from a tendency of $\boldsymbol{X}_a$ in the unforced system

$$\frac{d\boldsymbol{X}_a}{dt} + \boldsymbol{L}\boldsymbol{X}_a = 0 \quad , \tag{1}$$

where $\boldsymbol{L} \equiv \boldsymbol{L}(\boldsymbol{X}_c)$. While $\boldsymbol{L}$ can be constructed using the nonlinear model with infinitesimal perturbation (cf. Hoskins and Karoly 1981), the present model has been exactly linearized about the basic state (see Watanabe and Kimoto 2000, 2001 for mathematical expressions).

[1]The monthly index from 1950 onward is obtained from the Climate Prediction Center web site `http://www.cpc.noaa.gov/products/precip/CWlink/daily_ao_index/ao_index.html`.

The model variables are represented by spherical harmonics which has the horizontal resolution of T21 while vertically discretized using a finite difference on to 11 σ levels. Note that this vertical resolution may be poor to resolve the stratosphere while it has five layers below $\sigma = 0.8$, which is the same spacing as the 20–level model used by Kimoto et al. (2001).

The model includes three dissipation terms: a biharmonic horizontal diffusion with the damping timescale of 1 day for the smallest wave, very weak vertical diffusion (damping time scale of 1000 day) to remove a vertical noise arising from finite difference, and the Newtonian damping and Rayleigh friction as represented by a linear drag. The last two terms have a damping timescale of 1 day below the boundary layer ($\sigma \geq 0.9$) which mimics the turbulent fluxes and friction near the surface, and 2 day at the top level ($\sigma = 0.02$) that prevents a false wave reflection at the boundary. Inbetween, the $(10 \text{ day})^{-1}$ Newtonian cooling and $(15 \text{ day})^{-1}$ Rayleigh friction are applied, which are changed in section 3e to examine the sensitivity of singular vectors to them. Note that the boundary layer damping adopted here is strong enough to neutralize baroclinic instability waves in the system. Indeed, an eigenanalysis indicates that no unstable mode emerges at any frequency, with the dissipation terms described above (results are not shown).

The basic state is adopted from the zonally varying, winter climatology of the NCEP reanalysis. Since we focus on the large–scale variability, the zonal wavenumber is truncated at six. It should be noted that even with this truncation the matrix $\boldsymbol{L}$ has a rank of 8262 which is not easy to handle.

c. Singular mode theory

To relate the observed low–frequency variability as defined by EOFs of the covariance matrix with modes of the dynamical operator $\boldsymbol{L}$, we first assume that the tendency of $\boldsymbol{X}_a$ is small on seasonal or longer timescale hence Eq.(1) is modified to a steady version with external forcing $\boldsymbol{f}$ which is unknown. For more general arguments let us write a steady problem with a matrix

$\boldsymbol{A}$ instead of $\boldsymbol{L}$ as

$$\boldsymbol{A}\boldsymbol{X} = \boldsymbol{f} \quad . \tag{2}$$

The covariance matrix of $\boldsymbol{X}$ may be obtained by operating its transpose $\boldsymbol{X}^{\mathrm{T}}$ and taking an ensemble average denoted as $\langle \ \rangle$. Namely,

$$\begin{aligned} \boldsymbol{C} &\equiv \langle \boldsymbol{X}\boldsymbol{X}^{\mathrm{T}} \rangle \\ &= (\boldsymbol{A}^{\mathrm{T}} \langle \boldsymbol{f}\boldsymbol{f}^{\mathrm{T}} \rangle \boldsymbol{A})^{-1} \end{aligned} \tag{3}$$

In the simplest case which we consider, the forcing is assumed to be random in space, i.e., $\langle \boldsymbol{f}\boldsymbol{f}^{\mathrm{T}} \rangle = \boldsymbol{I}$. Although the forcing is in reality not spatially random, which will be discussed later, this assumption results in

$$\boldsymbol{C} = (\boldsymbol{A}^{\mathrm{T}}\boldsymbol{A})^{-1} \quad . \tag{4}$$

The above equation indicates that the covariance matrix $\boldsymbol{C}$ and $\boldsymbol{A}^{\mathrm{T}}\boldsymbol{A}$ share common eigenvectors but their eigenvalues are inversely correlated, leading to the *most dominant mode of* $\boldsymbol{C}$ *corresponds to an eigenmode with the smallest eigenvalue.*

Eigenfunctions of $\boldsymbol{A}^{\mathrm{T}}\boldsymbol{A}$ are obtained from the singular value decomposition (SVD) of $\boldsymbol{A}$, defined as

$$\boldsymbol{A} = \boldsymbol{U}\Sigma\boldsymbol{V}^{\mathrm{T}} \quad , \tag{5}$$

where

$$\boldsymbol{V} = (\boldsymbol{v}_1, \boldsymbol{v}_2, \boldsymbol{v}_3, ..., \boldsymbol{v}_i, ..., \boldsymbol{v}_N) \quad , \quad \boldsymbol{U} = (\boldsymbol{u}_1, \boldsymbol{u}_2, \boldsymbol{u}_3, ..., \boldsymbol{u}_i, ..., \boldsymbol{u}_N)$$

consist of N orthonormal vectors, called the v–vector (or the right singular vector) and the u–vector (or the left singular vector), respectively. Σ is a diagonal matrix, $\Sigma = \mathrm{diag}(\sigma_1, \sigma_2, \sigma_3, ..., \sigma_i, ..., \sigma_N)$, which contains real positive singular values σ_i (ordered as $\sigma_1 < \sigma_2 < ... < \sigma_N$).

Substituting Eq.(5) into Eq.(4) readily yields

$$\boldsymbol{C} = \boldsymbol{V}\Sigma^{-2}\boldsymbol{V}^{\mathrm{T}} \quad . \tag{6}$$

This means that $\boldsymbol{V}$ is identical to the eigenvector of $\boldsymbol{C}$ and $\boldsymbol{A}^{\mathrm{T}}\boldsymbol{A}$ while inverse square of the singular value corresponds to the eigenvalue of $\boldsymbol{C}$, suggesting that the leading mode of observed low–frequency variability is related by $\boldsymbol{v}_1$ of the matrix $\boldsymbol{L}$ in terms of the spatial structure.

What is the relationship between singular modes ($\boldsymbol{V}$ and $\boldsymbol{U}$) and eigenmodes of the normal mode form such as Eq.(1)? Branstator (1985) and Dymnikov (1988) have discussed this question in detail. Let $\boldsymbol{A}$ be decomposed into eigenvalues/eigenvectors (designated as Λ and $\boldsymbol{E}$). If $\boldsymbol{A}$ is not self–adjoint, as is $\boldsymbol{L}$, $\boldsymbol{E}$ is not orthogonal matrix, but orthogonal to $\boldsymbol{E}_a$, eigenvectors of the adjoint of $\boldsymbol{A}$. Therefore, multiplying $\boldsymbol{E}_a$ to the both sides of the normal mode expansion of $\boldsymbol{A}$ leads to a set of orthogonal matrices

$$\boldsymbol{A}\boldsymbol{E} = \Lambda\boldsymbol{E}_a \quad . \tag{7}$$

Comparing Eq.(7) with Eq.(5) indicates that the v– and u–vectors correspond to the eigenvectors of $\boldsymbol{A}$ and its adjoint, respectively, and the singular value is equal to the positive root of the complex eigenvalues (Itoh and Kimoto 1999). Thus, the singular mode with the smallest singular value, $\boldsymbol{v}_1$, may be interpreted as a resonant mode which has the smallest modulus in the conventional normal mode analysis. The growth rate of the singular mode is the closest to neutrality if the mode is assumed to be stationary, so that in this sense we refer a pair of $\boldsymbol{v}_1$ and $\boldsymbol{u}_1$ to as the *neutral mode* hereafter. Similar argument is also proposed by Marshall and Molteni (1993) and Goodman and Marshall (2003), in which they call $\boldsymbol{v}_1$ the neutral vector. The use of the neutral mode in a forced problem for $\boldsymbol{L}$, however, requires us to *a priori* know that the eigenmodes of $\boldsymbol{L}$ are all stable, or at least stable for the frequency lower than the timescale considered. For example, if we focus on a dynamical origin of the low–frequency variability as detected in seasonal mean anomaly fields (cf. Fig. 1), the neutral mode theory can be applied only when no unstable eigenmodes of $\boldsymbol{L}$ emerge on the seasonal or longer timescales.

Otherwise, the unstable mode will dominate the steady state response (Simmons et al. 1983; Branstator 1985). As mentioned in the previous section, the linear matrix of the LBM is, with a reasonable magnitude of dissipation, stable.

The neutral mode theory is relevant even if the forcing $\boldsymbol{f}$ is not spatially white. The forced steady response $\boldsymbol{X}$ is expressed from Eqs. (5) and (2) as

$$\begin{aligned} \boldsymbol{X} &= \boldsymbol{V}\Sigma^{-1}\boldsymbol{U}^{\mathrm{T}}\boldsymbol{f} \\ &= \Sigma_i^{\mathrm{N}}\boldsymbol{v}_i\frac{(\boldsymbol{u}_i,\boldsymbol{f})}{\sigma_i} \quad , \end{aligned} \tag{8}$$

where $(\boldsymbol{u}_i,\boldsymbol{f})$ denotes an inner product between the i–th u–vector and the forcing. Equation (8) is one of the major consequences of the singular mode theory, which tells us that a forced steady response is dominated by the v–vector of i–th singular mode that has either the smallest σ_i or the largest projection of $\boldsymbol{f}$ onto $\boldsymbol{u}_i$. It is therefore expected that the largest response will occur if the forcing vector is parallel to $\boldsymbol{u}_1$. On this regard, the u–vector is called the *optimal forcing* to the corresponding v–vector.

In the following sections, the spatial structure of the neutral mode ($\boldsymbol{v}_1$) and its optimal forcing ($\boldsymbol{u}_1$) will be presented. By referring to Eq. (8), one may think it as trivial that $\boldsymbol{v}_1$ has a similar spatial pattern to the leading EOF of observed fields, such as the AO. It is, however, non–trivial since the covariance matrix $\boldsymbol{C}$ is in nature constructed by the state vector evolving in the nonlinear system. The relevance and implication of the singular vectors in a simple nonlinear system is illustrated in the Appendix (see also Marshall and Molteni 1993).

3 Singular vectors and the dynamics

a. Neutral mode

Following the theory described in section 2c, the SVD is performed to the dynamical operator $\boldsymbol{L}$. It is obvious from the previous argument and Eq.(6) that the mode which we should focus

on is the v–vector of the neutral mode, $\boldsymbol{v}_1$, that is characterized by the smallest singular value σ_1. Figure 2 shows the inverse of singular values for the first 50 modes. It is found that the singular values for the first three modes are especially small compared to others. For example, σ_1^{-1} is six times larger than σ_{50}^{-1} in Fig. 2, and more than one order larger than the most of the rest singular values (not shown). In fact, the condition number $\sigma_{\max}/\sigma_{\min}$ is $O(10^6)$, which is equivalent to the inviscid case of the barotropic model computation and much larger than the case with realistic dissipation (Navarra 1993), indicating that the neutral mode is more singular than the leading singular mode that would be obtained by the barotropic model.

Shown in Fig. 3 are the height anomaly at $\sigma = 0.35$ (designated as $Z_{0.35}$), zonal–mean zonal wind and E–P fluxes, all associated with $\boldsymbol{v}_1$. In order to compare the spatial structure and the wave–zonal flow interaction with those of AO anomalies, Fig. 3 is drawn in the same manner as Fig. 1. The height anomaly has positive centers over eastern US, Europe and the North Pacific while negative centers over Greenland and Alaska. Except for the negative anomaly over Alaska, these centers roughly coincide those of the observed AO (Fig. 1a). At the same time, several discrepancies are found: positive height anomalies are too weak over Europe and shifted to the west over the Pacific, negative height anomaly that is not observed exists around 170°W, 25°N. Nevertheless, the spatial correlation between Figs. 1a and 3a over the Northern Hemisphere (20°–90°N) is +0.68, which indicates a good agreement between the neutral mode and the AO.

As expected from the zonally elongated structure of $Z_{0.35}$, a set of zonal–mean westerly and easterly anomalies is found near 65°N and 35°N, respectively (Fig. 3b). The maximum level of the zonal wind anomaly is lower than the AO, likely due to stronger damping at the upper boundary. The E–P fluxes are also similar to the observations (Fig. 1b) in terms of the direction and magnitude while the maximum is shifted to the north, which results in a disagreement between the flux convergence and the maximum easterly anomaly. As expected from the theory, a least– damped eigenmode reveals a quite similar structure to Fig. 3 (not

shown).

Low–level temperature anomalies are also compared in Fig. 4. Again, the overall pattern of the neutral mode (Fig. 4b) resembles the AO temperature anomaly (Fig. 4a). The temperature anomalies over the Atlantic sector between 90°W and 30°E are especially in good agreement both for the amplitude and location while the warming over eastern Eurasia is somewhat moved to the east in Fig. 4b. The cooling over Alaska is too strong in the neutral mode, but the location matches the observation. It is apparent that the overestimated cooling around Alaska leads to large height errors aloft (Fig. 3a).

Spatial patterns for another two singular vectors, which have relatively similar singularity to the neutral mode (Fig. 2), are also well organized and correspond to known dominant teleconnection patterns. The second v–vector ($\boldsymbol{v}_2$) reveals an arching structure from the subtropical Pacific, which is quite reminiscent of the Pacific/North American (PNA) pattern (Fig. 5). Because of its structure, polar projection is not used for presentation. The observed PNA pattern, obtained by regression on to the index following Wallace and Gutzler (1981), is well defined by four centers of action in the 500 hPa height anomalies (Fig. 5a) which accompany low–level cooling over Siberia, central North Pacific Ocean, and southeastern US while warming over Canada (Fig. 5b). These features are found in $\boldsymbol{v}_2$ as well (Figs. 5c and 5d) although the Pacific height anomalies are somewhat shifted to the west. This similarity between $\boldsymbol{v}_2$ and the PNA pattern is consistent with Branstator (1990) who obtained a PNA–like atmospheric response dominating among a number of steady solutions forced by spatial random noises. Feldstein (2002) also points out the growing stage of the PNA accomplished by an energy conversion from the non–zonal time–mean state, supporting that the prototype of the PNA can be obtained in the present analysis.

The $Z_{0.35}$ anomaly associated with the third v–vector, $\boldsymbol{v}_3$, is presented in Fig. 6, which is characterized by a zonal wavenumber two with negative anomalies over extratropical land regions and positive anomalies inbetween. As deduced from Fig. 6, $\boldsymbol{v}_3$ reveals near–surface

cooling over most of the midlatitude continents (not shown). These height and temperature patterns are remarkably similar to the cold ocean–warm land (COWL) pattern as defined by means of surface temperature (Wallace et al. 1995; Broccoli et al. 1998).

b. Linear budgets

In order to understand the dynamical balance in the neutral mode, we use the so–called planetary wave model (PWM), which is a linear model same as that described in section 2b, except for the zonally uniform basic state. Let $\boldsymbol{L}$ be decomposed as $\boldsymbol{L} = \boldsymbol{B} + \boldsymbol{D}$, where $\boldsymbol{D}$ contains elements independent of the basic state, such as the dissipation and Coriolis terms, and assuming that σ_1 is sufficiently small, the following balance may be satisfied in terms of $\boldsymbol{v}_1$:

$$(\overline{\boldsymbol{B}} + \boldsymbol{D})\boldsymbol{v}_1^* \simeq \boldsymbol{B}^*\boldsymbol{v}_1 \qquad , \tag{9}$$

where the overbars and asterisks denote zonally uniform and eddy (deviation from the zonal mean) components, respectively, and

$$\overline{\boldsymbol{B}} \equiv \boldsymbol{B}(\overline{\boldsymbol{X}}_c) \quad , \quad \boldsymbol{B}^* \equiv \boldsymbol{B}(\boldsymbol{X}_c^*) \quad .$$

Since v–vector is not the exact solution of steady unforced equations, Eq.(9) represents an approximate balance. When $\boldsymbol{v}_1$ on the right–hand–side of Eq.(9) is divided into its zonal average, $\overline{\boldsymbol{v}}_1$, and eddies, $\boldsymbol{v}_1^*$, we obtain steady eddy responses associated with the zonal–mean and eddy parts of the neutral mode as

$$\boldsymbol{X}_{\mathrm{ZW}}^* = (\overline{\boldsymbol{B}} + \boldsymbol{D})^{-1}\boldsymbol{B}^*\overline{\boldsymbol{v}}_1 \quad , \quad \boldsymbol{X}_{\mathrm{WW}}^* = (\overline{\boldsymbol{B}} + \boldsymbol{D})^{-1}\boldsymbol{B}^*\boldsymbol{v}_1^* \quad . \tag{10}$$

The subscripts 'ZW' and 'WW' in Eq.(10) stand for the eddy anomalies induced by the coupling between the zonal mean state of $\boldsymbol{v}_1$ and climatological stationary waves, and between anomalous (i.e. $\boldsymbol{v}_1^*$) and climatological waves, respectively. Note that the former process, often referred to as the zonal–wave coupling, has been a central part of the AO dynamics discussed

by DeWeaver and Nigam (2000b) and Kimoto et al. (2001), which includes the horizontal temperature advection at low level as shown by Thompson and Wallace (2000).

Figures 7a and 7b show $Z^*_{0.35}$ anomaly of the neutral mode and of the steady PWM response ($\boldsymbol{X}^*_{\rm ZW} + \boldsymbol{X}^*_{\rm WW}$), respectively. Regardless of several small discrepancies, the PWM response fairly well reproduces the eddy component of the neutral mode, indicating that the balance in Eq.(9) is roughly satisfied. As shown in Fig. 3b, the zonally averaged eddy momentum fluxes associated with the neutral mode, $\overline{u^*_a v^*_c + u^*_c v^*_a}$, has a positive maximum around 60°N, which is followed by the PWM response although the magnitude is slightly underestimated (Fig. 7c). The eddy height anomaly shown in Fig. 7b is decomposed into $\boldsymbol{X}^*_{\rm ZW}$ and $\boldsymbol{X}^*_{\rm WW}$, which compare the relative importance of the zonal–wave and wave–wave coupling processes (Figs. 7d and 7e). Consistent with previous results (DeWeaver and Nigam 2000b; Kimoto et al. 2001), the zonal–wave coupling accounts for the substantial part of height anomalies over the Atlantic and northern Eurasia (Fig. 7d). Cooling (warming) over Greenland (Europe) near the surface (Fig. 4b) is also attributed to this process. On the other hand, eddy height anomalies over the Pacific, North America, and southern Eurasia are found to be induced by the coupling between climatological stationary waves and wave components of the neutral mode (Fig. 7e). A simple consideration of the vorticity budget indicates that the four positive/negative centers between 30°E and 150°W are mostly balanced by the climatological trough associated with the Pacific jet, located to the the north of Japan. These diagnoses reveal that, for the total eddy structure of the neutral mode, both processes appear to be equally important. Corresponding eddy momentum transports are northward for both $\boldsymbol{X}^*_{\rm ZW}$ and $\boldsymbol{X}^*_{\rm WW}$ while the former has a broader meridional shape and a weaker maximum compared to the latter (Fig. 7f). Note that $\boldsymbol{X}^*_{\rm WW}$ does not depend on the zonal mean anomaly, so that the northward eddy momentum transport of $\boldsymbol{X}^*_{\rm WW}$ acts as one–way forcing for the anomalous zonal–mean flow $\overline{u}_a$ while that of $\boldsymbol{X}^*_{\rm ZW}$ positively feeds back to $\overline{u}_a$, which contributes to amplify the neutral mode structure. It should be noted that the net northward momentum transport associated with $\boldsymbol{X}^*_{\rm WW}$ (Fig.

7f) results from a tilted trough over Siberia (Fig. 7e) while the other momentum fluxes cancel with each other along the latitudinal circle (not shown).

Comparison is also made for the wave–zonal flow interaction with the observational counterpart. Figure 8a shows $\overline{u_a^* v_c^* + u_c^* v_a^*}$ at 300 hPa associated with the AO (solid line) and the neutral mode obtained by Kimoto et al. (2001) (dashed line). The latter comes from a mode selected solely by the wave–zonal flow interaction (cf. section 1), which has a broad positive flux in midlatitudes as in the observation but the amplitude less than half. On the other hand, the momentum flux associated with the present neutral mode (Fig. 8b, solid line) has a comparable magnitude to the AO, except for the maximum shifted to the north by 15°as confirmed in Fig. 3b. Superimposed on Fig. 8b is the momentum flux associated with $\boldsymbol{X}^*_{\mathrm{ZW}}$ (dashed line) which is the same as shown in Fig. 7f but at different level ($\sigma = 0.35$). It is evident that the two dashed lines in Fig. 8 are nearly identical, which implies that the neutral mode presented here includes the wave–zonal flow interaction at work in the same manner as the mode computed by Kimoto et al. (2001).

c. Inter–basin connection

In the previous section we showed that the Atlantic (Pacific) part of the neutral mode is roughly induced by the zonal–wave (wave–wave) coupling, which indicates the crucial role of the climatological stationary waves in maintaining the $\boldsymbol{v}_1$ structure against dissipation. This diagnosis is based on the steady dynamical balance but not on the time dependent process. Similarly, the singular mode analysis implies that $\boldsymbol{v}_1$ has the longest timescale among other modes *if* it exists at initial time. In other words, the neutral mode structure might be obtained even when the Atlantic and Pacific parts are independently evolving in time. As will be shown below, however, the $\boldsymbol{v}_1$ anomalies over the two ocean basins are indeed coupled. In order to illustrate it, LBM is used in a time dependent manner in this subsection.

While time integration of the model appears a suitable way to examine the development of the neutral mode structure, we cannot use arbitrary initial perturbations since the neutral

mode is not an unstable growing mode unlike the barotropic instability (Simmons et al. 1983). Instead, we adopt $\boldsymbol{v}_1$ itself as the initial perturbation, with which Eq.(1) is integrated in time, but the perturbation is confined to one ocean basin (i.e. Atlantic or Pacific region) in order to detect its influence to another ocean basin. Figure 9a–d shows the time evolution of the $Z_{0.35}$ and associated meridional wind ($v_{0.35}$) anomalies at each day, initially starting from the $\boldsymbol{v}_1$ anomalies over the Atlantic hemisphere (110°W–70°E). Note that a factor has been multiplied before illustrating in order to remove decay components of $\boldsymbol{v}_1$.

It is clearly found that a train of wave packets is rapidly established over Eurasia and the North Pacific during day 2–4 while the anomalies remain roughly the same over the Atlantic and Europe (Fig. 9b–d). Analysis of the wave activity flux (not shown) reveals that this wave train emanates from the negative vorticity source around Middle East accompanied by northerly wind anomalies over India (Fig. 9a) and propagates along the Asian jet (cf. gray contours in Fig. 9d) with the phase speed of 40°/day. The rapid establishment of the Eurasia–Pacific anomalies is indicative of the wave energy propagating along the subtropical jet which acts as a Rossby waveguide (Hoskins and Ambrizzi 1993). While the maximum group velocity on the Asian jet, assumed $u_c = 40$ m s^{-1}, is estimated as $|\boldsymbol{c}_g| \simeq 70°$/day which is much faster than the propagation speed found in Fig. 9b–d, $\boldsymbol{c}_g$ has a meridional component in the waveguide as well. It should be noted that the wave packet is developed such that the southerly anomaly over East Asia contributes to bring the low–level warming as confirmed by the $Z_{0.35}$ anomalies in Fig. 9c–d. Both of these $v_{0.35}$ and $Z_{0.35}$ anomalies over Eurasia and the North Pacific are quite similar to the observed AO anomalies (Fig. 9i), suggesting that the Atlantic part of $\boldsymbol{v}_1$ anomalies helps developing the hemispheric structure of the neutral mode. A similar downstream extension of the stationary waves trapped on the Asian jet is identified in association with the observed NAO (Branstator 2002; Watanabe 2003).

When the initial $\boldsymbol{v}_1$ perturbation is limited to the Pacific hemisphere (70°E–110°W), the inter–basin connection is not as clear as the Atlantic case. The wave packet seems to propagate

eastward along the Atlantic jet (Fig. 9e–h), which is much slower than that found in Fig. 9a–d. Nevertheless, $v_{0.35}$ and $Z_{0.35}$ anomalies over the North Atlantic developed at day 4 (Fig. 9h) resemble well the $\boldsymbol{v}_1$ anomalies (Fig. 9a). Both of the time sequences presented in Figs. 9a–d and 9e–h thus indicate a presence of the inter–basin connection in the neutral mode, i.e., anomalies in one hemisphere tend to excite those in another hemisphere via the wave energy propagation along the jetstreams. The timescale of the inter–basin coupling is order of a few days, which is rapid enough compared to the dissipative timescale of 10–15 days employed in the LBM.

d. Role of baroclinic process

As mentioned in the introduction, there have been attempts to compute singular vectors for the barotropic vorticity equation linearized about the observed upper–level flow (Navarra 1993; Metz 1994; Bladé 1996). However, the neutral mode in their models does not necessarily resemble the leading EOF of either observed or the model generated fields, and furthermore, the structure of the singular mode was shown to be sensitive to the damping parameter and the choice of an equivalent barotropic level. On the other hand, structure of the neutral mode obtained here shows a remarkable similarity to the observed leading EOF (i.e. the AO) and is not sensitive to the damping parameters (cf. next section). This difference suggests that, even though most of teleconnection patterns including the AO are equivalent barotropic, barotropic models lack processes which significantly contribute to form the AO–like horizontal structure. Therefore, the diagnostic analysis for the neutral mode is extended to find out causes that lead to differences between the barotropic and baroclinic model results.

In Eq.(10) decomposition of $\boldsymbol{v}_1$ is modified to $\boldsymbol{v}_1 = \boldsymbol{v}_1^{\rm bt} + \boldsymbol{v}_1^{\rm bc}$, where $\boldsymbol{v}_1^{\rm bt}$ and $\boldsymbol{v}_1^{\rm bc}$ are barotropic and baroclinic components of the neutral mode, respectively. Each component is defined as

$$\boldsymbol{v}_1^{\rm bt} = (u^{\rm bt}, v^{\rm bt}, 0, Ps^{\rm bt}) \quad , \quad \boldsymbol{v}_1^{\rm bc} = (u^{\rm bc}, v^{\rm bc}, T, Ps^{\rm bc}) \quad ,$$

and

$$u^{\rm bt} = -\partial_y \tilde{\psi} \quad , \quad v^{\rm bt} = \partial_x \tilde{\psi} \quad , \quad Ps^{\rm bt} = \rho f \tilde{\psi} \quad , \tag{11}$$

$$u^{\rm bc} = u - u^{\rm bt} \quad , \quad v^{\rm bc} = v - v^{\rm bt} \quad , \quad Ps^{\rm bc} = Ps - Ps^{\rm bt} \quad , \tag{12}$$

where u, v, T, Ps, and ψ are all the anomalies associated with the neutral mode and $\tilde{(\ )}$ denotes the vertical average. Steady $Z^*_{0.35}$ responses as computed by $(\overline{\boldsymbol{B}} + \boldsymbol{D})^{-1}\boldsymbol{B}^*\boldsymbol{v}_1^{\rm bt}$ and $(\overline{\boldsymbol{B}} + \boldsymbol{D})^{-1}\boldsymbol{B}^*\boldsymbol{v}_1^{\rm bc}$ are displayed in Figs. 10a and 10b, respectively. They show that the magnitude of the response is comparable between the two, although the $Z^*_{0.35}$ anomaly associated with the barotropic component has a larger spatial extent. While the height anomaly pattern in Fig. 10a shows higher similarity to the total eddy field (cf. Fig. 7b), negative height response over northwestern Canada is much enhanced, in addition to the negative center over the North Atlantic is shifted eastward. These discrepancies are compensated by the steady response to the baroclinic component (Fig. 10b). It should be noted that these response patterns were not seriously altered when $\boldsymbol{v}_1^{\rm bt}$ is defined as an equivalent barotropic component of $\boldsymbol{v}_1$ (not shown).

Since the anomaly fields associated with $\boldsymbol{v}_1^{\rm bc}$ are indicative of the vortex stretching and/or shrinking from the point of the potential vorticity view, those accounting for a significant portion of the total eddy fields implies that a baroclinic process has a certain role in maintaining the neutral mode structure. The barotropic model which lacks such a process is anticipated to produce a neutral mode less similar to the AO–like spatial pattern.

e. *Sensitivity to damping*

Given a basic state which employs the observed winter climatology, dissipation terms are only changeable elements in the linear operator $\boldsymbol{L}$. In particular, the Rayleigh friction and Newtonian damping as represented by a linear drag are difficult to determine the correct values. While the drag coefficients below the planetary boundary layer should be strong enough to mimic the surface friction and heat flux damping, the drag in the free atmosphere that would implicitly include nonlinear effects (Ting and Held 1990) can be varied between weeks. In this

section, the extent to which the neutral mode structure is sensitive to the choice of damping coefficients is investigated.

In Fig. 11a vertical profiles of the damping coefficients are shown together with those for the standard Rayleigh friction (denoted as γ) and Newtonian cooling (α). Except for the extreme case of uniform $(1\ \mathrm{day})^{-1}$ damping, difference among the profiles is only made for $0.1 \leq \sigma < 0.9$. As described in section 2b, the tropospheric values of γ and α in the reference case have the damping timescale of 15 and 10 days, respectively. For the preliminary test, the profile for α is varied but γ kept fixed, then singular vectors are repeatedly computed. The inverse singular values for 7 cases, each of which adopts a different α profile, are displayed in Fig. 11b. Note that the uppermost curve is the result without Newtonian damping for $0.1 \leq \sigma < 0.9$ (not shown in Fig. 11a). It is clearly found in Fig. 11b that the singular value of the leading mode (σ_1) tends to be selectively smaller as α becomes smaller. This change in σ_1 is reasonable if we interpret the neutral mode as a resonant mode in the eigenanalysis (cf. section 2c). Similar results are obtained when γ varies but α prescribed (not shown).

Figure 11b indicates that the singular value of the neutral mode is sensitive to the choice of either α or γ. In order to illustrate how the spatial pattern of the mode is affected by these parameters, we compute the hemispheric (20°–90°N) spatial correlation between $Z_{0.35}$ anomalies of the observed AO and the neutral mode for various sets of linear damping, then plot the coefficients as a function of α and γ (Fig. 12). Before calculating the correlation, the observed anomalies were interpolated onto the model σ levels, which provide the AO $Z_{0.35}$ anomaly. The correlation is generally higher (lower) for either α or γ is smaller (bigger) although the sensitivity is slightly larger to the thermal damping. A set of standard parameters is also indicated by star in the figure, where the neutral mode structure is not the best correlated with the AO. The highest correlation almost reaches +0.80 when the Rayleigh friction is $(30\ \mathrm{day})^{-1}$ and no Newtonian damping is applied to the troposphere. In the area of reasonable damping timescale of $(10\text{–}30\ \mathrm{day})^{-1}$ the spatial correlation ranges +0.65–0.75, which exhibits

that the neutral mode structure in terms of the v–vector is quite robust for the realistic range of damping. Since the mode without the thermal or mechanical damping is conspicuously singular (Fig. 11b) hence closer to a purely resonant mode, the result shown in Fig. 12, i.e., that higher correlation takes place for weaker damping, suggests that the AO spatial structure essentially comes from a spatial resonance of the climatological state. Although the capability of the neutral mode will be broken if unstable, low–frequency eigenmode emerges for a set of weak damping parameters examined in Fig. 12, such a situation has not happened because of strong damping prescribed in the boundary layer.

4 Optimal forcing

In the previous sections, we focused on to examine the v–vector of the neutral mode, which determines the spatial structure of forced steady response, as represented by Eq. (8). At the same time Eq. (8) shows that the extent to which the singular mode is excited depends on the projection of a forcing vector onto the optimal forcing, i.e., u–vector. Specifying an effective forcing to the AO will help understanding its predictability, so that the optimal forcing of the neutral mode, $\boldsymbol{u}_1$, is delineated in this section.

Since a major forcing to the atmospheric low–frequency variability is thought to result from diabatic processes, the thermal component of $\boldsymbol{u}_1$ is presented in Fig. 13, which shows the optimal diabatic heating and cooling to $\boldsymbol{v}_1$ at the lower (Fig. 13a) and upper (Fig. 13b) levels, respectively. In the lower troposphere, the optimal forcing is concentrated on the extratropics, where a heating is found over eastern Eurasia and Iceland while a cooling over the Aleutian islands and Labrador Sea, respectively. The forcing pattern over the North Atlantic is reminiscent of the surface temperature anomaly formed by the horizontal advection associated with the positive phase of the NAO. On the other hand, a positive thermal forcing over eastern Eurasia is consistent with the results by Watanabe and Nitta (1998) who found that the lesser snow cover in autumn over this region can force the AO–like height anomalies in the subsequent

winter through the anomalous shortwave heating due to lower surface albedo. It is noteworthy that, in the upper troposphere, a dominant thermal forcing appears over the tropics in addition to the extratropics. In particular, heating over the Indian Ocean and cooling near Philippines are prevailing, suggesting that the anomalous diabatic forcing associated with changes in the tropical convective activity can also be optimal in exciting the neutral mode.

Relative influence of the tropical and extratropical thermal forcings is examined by means of the LBM. Unlike the diagnosis performed in section 3b, we use the dynamical operator $\boldsymbol{L}$ and compute a steady response as $\boldsymbol{X} = \boldsymbol{L}^{-1}\boldsymbol{u}_1$, where $\boldsymbol{u}_1$ only contains the temperature component. Shown in Fig. 14a is the steady $Z_{0.35}$ response to the optimal thermal forcing over the whole globe. The magnitude of the forcing is adjusted such as to produce a response with the comparable amplitude to $\boldsymbol{v}_1$. Despite the fact that the optimal forcing for ζ, D, and Ps is not included, the steady $Z_{0.35}$ response reproduces well the neutral mode shown in Fig. 3a. Given this relevance of the optimal thermal forcing, the steady response is again computed to the same forcing but restricted to the tropical (20°S–20°N) or the extratropical (20°–90°N) bands. The $Z_{0.35}$ response to the tropical forcing (Fig. 14b) reveals a negative (positive) anomalies in polar regions (midlatitudes) but the amplitude is much weaker than the total response (Fig. 14a). On the other hand, the $Z_{0.35}$ anomaly induced by the extratropical forcing (Fig. 14c) is similar to that in Fig. 14a in terms of the amplitude and spatial pattern. This result indicates that, if the forcing has the magnitude relatively the same as $\boldsymbol{u}_1$ between the tropics and the extratropics, the tropics impacts the steady response much weaker than the extratropics. It may imply a weak sensitivity of the neutral mode to the tropical diabatic heating, but in nature the variance of the thermal forcing would be much larger in the tropics, so that the tropical forcing will excite the atmospheric response much stronger than the anomalies shown in Fig. 14b.

5 Summary and discussion

In this study, an attempt has been made to examine dynamical origin for the low–frequency variability of the extratropical atmosphere by means of singular modes of the primitive equation model linearized about the boreal winter climatology. Of particular interest is the spatial structure (called v–vector) of the near–neutral mode, which is regarded as a least–damped mode in the conventional eigenanalysis. Since the leading statistical EOF of the observed fields, the AO, has extensively been discussed in terms of its physical relevance, we focused on whether the neutral mode has a similarity to the observed AO.

It turns out that the v–vector of the neutral mode ($\boldsymbol{v}_1$) does resemble the AO in many aspects (Figs. 3 and 4), suggesting that the hemispheric structure of the AO tends to be preferred by time–mean states of the atmosphere that includes zonal, as well as meridional and vertical, inhomogenieties. Another two modes which have the next smallest singular values ($\boldsymbol{v}_2$ and $\boldsymbol{v}_3$) appear to coincide the pronounced teleconnections as well, i.e. the PNA and COWL patterns respectively, reinforcing the above arguement. The neutral mode involves a positive wave–zonal flow feedback at work over the North Atlantic, consistent with previous studies (DeWeaver and Nigam 2000b; Kimoto et al. 2001), and additionally a coupling between anomalous (i.e. the neutral mode itself) and climatological stationary waves which appears crucial in forming the anomaly pattern over the North Pacific (Figs. 7 and 8). While the neutrality as measured by the inverse singular value varies following the strength of thermal and mechanical dampings, the spatial structure is found quite robust for a wide range of the damping timescales (Figs. 11 and 12). This strengthens the reliability of our neutral mode structure unlike singular modes obtained from a barotropic model which reveals a large sensitivity of the result to the choice of damping coefficient and a reference level (cf. Bladé 1996).

By referring to Eq.(6), one may consider it as not surprising that $\boldsymbol{v}_1$ resembles the leading statistical EOF, i.e., the AO. It is, however, not trivial because Eq.(6) has been used with the following assumptions: observed winter mean anomalies can be represented as *linear*, *steady*

atmospheric response to a *spatially random* external forcing. In nature, these assumptions are, of course, not guaranteed. The similarity between $\boldsymbol{v}_1$ and the AO not only justifies the above assumptions in part but also implies that the AO–like structure can be preferred even without processes excluded in the current system, such as the troposphere–stratosphere coupling and an interaction with transient disturbances.

As described in the introduction, this study aims at contributing to the AO/NAO debates in terms of their physical significance. Results of the singular vector analysis presented in this study appear to support the notion by Thompson and Wallace (1998, 2000), that is, the AO is regarded as a dynamically consistent mode of variability which is preferred by the climatological winter atmospheric state. However, we never say that the NAO is apparent; given that an interaction between the NAO and the Atlantic storm track acts to enhance the regional structure of the NAO (Hurrell and van Loon 1997; Watanabe and Kimoto 2000), it is highly plausible that the neutral mode more looks like the NAO if the feedback from changes in storm tracks can be incorporated into the dynamical operator. This is a hard challenge for the linear dynamical modeling, but we have developed such a parameterization and indeed obtain a neutral mode that is similar to the NAO without climatological stationary eddies (Jin et al. 2003a, 2003b). Thus we may conclude that both the AO and NAO are dynamically relevant modes but with a slightly different reason. The hemispheric structure of the AO is primarily selected by a slow, or quasi–steady, component of the dynamical atmosphere, as suggested by the neutral mode in this study, while the regional structure of the NAO is perhaps generated and/or maintained through the coupling between slow and fast (i.e. storm track activity) components of the atmosphere.

The singular vectors are based on a linear dynamics, as well as the statistical EOF analysis to the observed fields. In a nonlinear perspective, efforts have been made to look for quasi stationary states or 'regimes' of the circulation in a probability density distribution of geopotential height fields (e.g. Kimoto and Ghil 1993; Corti et al. 1999). Recently, Monahan et al. (2001)

pointed out that three quasi stationary states found in the probability density function do not align on one straight axis unlike a simpler system (e.g. Lorenz system, see Appendix) and therefore the axis of the AO as defined by the principal components of the EOF1 necessarily represents a transition phase of these quasi stationary states but not the regimes themselves. This critique would also be applicable to the present dynamical analysis. Taking these arguments into consideration, we should note a restriction in interpreting our results: a dynamical consistency of the observed AO can be given by the neutral singular mode, which is relevant when the linear point of view is employed.

Singular modes consist of a set of v– and u–vectors. In the steady problem as examined here, the u–vector represents an optimal forcing pattern to the corresponding v–vector, while the former (latter) gives an initial condition (final state) in the time evolving, initial value problem as often employed in the numerical weather forecast. Thus the u–vector is as crucial as the v–vector in order to elucidate the predictability associated with the singular modes.

The optimal thermal forcing to the neutral mode shows that a deep heating over the tropical Indian Ocean can excite the positive phase of the AO–like structure (Fig. 13). While the sensitivity to the tropical heating appears small compared to the midlatitude forcing (Fig. 14), it is only if the thermal forcing has a similar magnitude over the tropics and the extratropics. Since the variance of the anomalous diabatic heating is generally larger over the tropics, the Indian Ocean heating to the neutral mode would be much effective than that suggested by Fig. 14. It is worth noting that this tropical heating is reminiscent of a finding by Hoerling et al. (2001) and Peterson et al. (2002), who showed that the recent positive trend in the NAO results from a gradual warming in the tropical Indian Ocean and the western Pacific. Simultaneously, the optimal thermal forcing reveals a shallow heating over eastern Eurasia (Fig. 13a), which is coincident with the fact that a surface shortwave heating over the region, induced by deficient autumn snow cover, can excite an AO–like atmospheric response (Watanabe and Nitta 1998).

The optimal forcing pattern to the neutral mode seems to be reasonable in referring to earlier

reports on the possible causes for the AO/NAO fluctuations. On the other hand, applying the optimal forcing to predictability studies yet contains a difficulty as well as an uncertainty. First, the direction toward which the singular modes are excited greatly depends on the forcing structure. In order for hindcasting the year–to–year variability of the AO using Eq. (8), it is necessary to estimate the accurate forcing anomaly, which is quite difficult though is possible (cf. DeWeaver and Nigam 2000b; Peterson et al. 2002). Second, the structure of the u–vector may not be as robust as the v–vector, due to its sensitivity to the basis of norm (Goodman and Marshall 2003). While we have used a L^2 norm to construct the linear operator matrix, the robustness of the u–vector as presented in section 4 should be verified with a different (e.g. energy) norm.

Acknowledgments

We thank M. Kimoto, H. Mukougawa, and S. Yoden for stimulating discussion. This work is partially supported by a Grant–in–Aid for Scientific Research from the Ministry of Education, Science, and Culture of Japan. FFJ is also supported by NOAA Grants GC99–234, GC01–229, GC01–246, and NSF Grant ATM-9615952.

APPENDIX

Singular vectors in the Lorenz system

As one of the simplest model of the atmospheric flow to which we apply the neutral mode analysis, we choose a well–known Lorenz's (1963) dynamical system, which consists of nonlinear equations for three variables:

$$dx/dt = -\sigma x + \sigma y$$

$$
\begin{aligned}
dy/dt &= -xz + rx - y \qquad (A1)\\
dz/dt &= xy - bz \qquad ,
\end{aligned}
$$

where $\sigma = 10.0$ and $b = 8/3$ following Lorenz (1963), and we set $r = 35.0$ according to the fact that this value higher than 24.7 yields a famous strange attractor that has no stable stationary solutions. While this model has originally been developed to mimic Rayleigh–Benard convection, it does not matter in the present analysis.

After integrating Eq. (A1) for 100,000 nondimensional time steps with an infinitesimal initial perturbation, EOF analysis was performed to the last 50,000 samples. Each of the resultant EOFs is indicated by a straight axis in Fig. A1 superimposed on the model trajectories. The leading EOF, which accounts for 62.3% of the total variance, is almost parallel to the $x - y$ plane and roughly straddles two unstable stationary solutions, $(x_s, y_s, z_s) = (\pm\sqrt{b(r-1)}, \pm\sqrt{b(r-1)}, r-1)$. The second EOF (33.2%) is quite close to the z axis, and more than 95% of the total variance is explained by these two EOFs. It should be noted that the first EOF represents a transition between two stationary states, indicating that the statistically derived 'mode' is dynamically relevant as well in this simple system.

We then linearize Eq. (A1) about a basic state (x_0, y_0, z_0), and compute singular modes of the linear operator matrix which forms

$$
\boldsymbol{L} = \begin{bmatrix} \sigma & \sigma & 0 \\ z_0 - r & 1 & x_0 \\ -y_0 & -x_0 & b \end{bmatrix} \qquad . \qquad (A2)
$$

The SVD is applied to this 3×3 matrix as described in section 2c, in which we again focus on the neutral mode, $\boldsymbol{v}_1$ and $\boldsymbol{u}_1$, that is characterized by the smallest singular value σ_1. While the basic state should be in principle given by one of the stationary solutions, in such a case singular modes are aligned on quite different axes from the EOFs, and two among the modes correspond to unstable oscillations evolving around the stationary state but not a

transition between the regimes (Marshall and Molteni 1993). On the other hand, when Eq. (A1) is linearized about the time–mean state of the nonlinear integration, which is analogous to the LBM computation carried out in this study, v–vectors of three singular modes reveal axes nearly identical to the statistical EOFs (Fig. A2). Inverse singular values for σ_1–σ_3 are 0.43, 0.38, and 0.068, respectively, so that $\boldsymbol{v}_1$ and $\boldsymbol{v}_2$ are closer to neutrality compared to $\boldsymbol{v}_3$. This result suggests the relevance to choose time–mean 'climatology' as the model basic state.

The Lorenz system contains two types of variabilities: high–frequency oscillations around the unstable stationary states and a low–frequency aperiodic fluctuation between regimes, the latter being selected by the EOF1. Since (x_s, y_s, z_s) are unstable, the singular mode or equivalent eigenmode automatically prefers the high–frequency oscillation when they are adopted as the basic state. In contrast, the time–mean 'climatology' is equally far from those regimes, therefore seems to be better in detecting the low–frequency regime transition as the neutral mode. However, the neutral mode around a basic state that has the equal distance to stationary states does not necessarily match the EOF1, as explained below.

Given that linearizing the Lorenz model about the climatology is justified in terms of the singular mode analysis, how the axis of the neutral mode is sensitive to a small deviation in the basic state from the climatology? To answer this question, we first define a plane spanned by the EOFs 1 and 2, and the singular modes are calculated with a basic state altered within the plane. Figure A3 represents inner products between the EOF1 and neutral mode $\boldsymbol{v}_1$, plotted on the EOF plane, superimposed on the trajectories projected on the plane. It is obvious that the sensitivity has a certain structure such that the neutral mode nearly assigns the same axis as the EOF1 when the basic state is in a small area centered on $(0, 4)$ corresponding to $(x_0, y_0, z_0) = (0, 0, r - 1)$, which is particularly sensitive to a small change of the basic state along the EOF2 axis (cf. shading in Fig. A3). Since the EOF2 axis is almost parallel to the z axis, Fig. A3 indicates that the EOF1 can be represented by $\boldsymbol{v}_1$ when z_0 is equal to, or lower than z_s, except for $x_0 \approx y_0 \approx 0$ where the neutral mode tends to represent the EOF2 (not

shown). Singularity of the neutral mode, as measured by σ_1^{-1} (thick lines in Fig. A3), follows maxima of the inner products.

Capability of the u–vector in predicting the behavior of trajectories is tested by integrating Eq. (A1) again but with a steady forcing $\boldsymbol{f} = (-5.4, 19.3, 0.0)$, where $\boldsymbol{f} \parallel \boldsymbol{u}_1$. In the nonlinear Lorenz system, it is known that steady forcing introduced brings changes in the probability density distribution of the trajectory (Palmer 1993). So what we should expect is that the trajectories forced by $\boldsymbol{f}$ are shifted toward the positive phase of the $\boldsymbol{v}_1$ axis. A comparison of the unforced and forced Lorenz attractors (Fig. A4) indeed shows it, encouraging to consider the optimal forcing pattern identified in section 4 as useful for the predictability of the AO–like circulation anomalies. As mentioned in section 2c, even for an arbitrary forcing we would be able to predict the direction to which the probability distribution is moved by evaluating the inner product $(\boldsymbol{u}, \boldsymbol{f})$.

The neutral mode in the Lorenz system and its implication may be summarized as follows.

- When the model is linearized about the time–mean 'climatological' state, the neutral mode of $\boldsymbol{L}$ agrees well with the EOF1, which represents the low–frequency transition between two stationary regimes.

- The u–vector can be used to predict changes in the probability density distribution of the trajectories, but not the state at a certain period.

The first point is consistent with Marshall and Molteni (1993), who has also examined the neutral mode in the Lorenz model. The above conclusions are positive parts of the neutral mode analysis. There is, however, a negative part, or uncertainty in the neutral mode, too.

- Whether the neutral mode can represent the statistical EOF1 is relatively sensitive to the basic state. Furthermore, the sensitivity is not isotropic; there is a certain direction of higher or lower sensitivity in the phase space.

Exploring factors which determine the unisotropic sensitivity as shown in Fig. A3 is important for fully developing the neutral mode theory, which should be done elsewhere. In more realistic model such as the LBM, it will be much harder to even identify the direction of the high sensitivity to the small deviation, or errors, in the basic state because of too many degrees of freedom. In addition, unlike in the Lorenz system, transition between multiple quasi–stationary states in the observed atmosphere may not be captured by the linear singular modes as well as the statistical EOF, leading to a difficulty in interpreting the neutral mode as discussed in section 5.

References

Ambaum, M. H. P., B. J. Hoskins, and D. B. Stephenson, 2001: Arctic Oscillation or North Atlantic Oscillation? *J.Climate*, **14**, 3495–3507.

Baldwin, M. P., and T. J. Dunkerton, 1999: Propagation of the Arctic Oscillation from the stratosphere to the troposphere. *J.Geophys.Res.*, **104**, 30937–30946.

Bladé, I., 1996: On the relationship of barotropic singular modes to the low–frequency variability of a general circulation model. *J.Atmos.Sci.*, **53**, 2393–2399.

Branstator, G., 1984: The relationship between zonal mean flow and quasi–stationary waves in the midtroposphere. *J.Atmos.Sci.*, **41**, 2163–2178.

Branstator, G., 1985: Analysis of general circulation model sea–surface temperature anomaly simulations using a linear model. Part II: Eigenanalysis. *J.Atmos.Sci.*, **42**, 2242–2254.

Branstator, G., 1990: Low–frequency patterns induced by stationary waves. *J.Atmos.Sci.*, **47**, 629–648.

Branstator, G., 2002: Circumglobal teleconnections, the Jet stream waveguide, and the North Atlantic Oscillation. *J.Climate*, **15**, 1893–1910.

Broccoli, A. J., N.-C. Lau, and M. J. Nath, 1998: The cold ocean–warm land pattern: Model simulation and relevance to climate change detection. *J.Climate*, **11**, 2743–2763.

Corti, S., F. Molteni, and T. N. Palmer, 1999: Signature of recent climate change in frequencies of natural atmospheric circulation regimes. *Nature*, **398**, 799–802.

Deser, C., 2000: On the teleconnectivity of the 'Arctic Oscillation'. *Geophys.Res.Lett.*, **27**, 779–782.

DeWeaver, E., and S. Nigam, 2000a: Do stationary waves drive the zonal–mean Jet anomalies of the northern winter? *J.Climate*, **13**, 2160–2176.

DeWeaver, E., and S. Nigam, 2000b: Zonal–eddy dynamics of the North Atlantic Oscillation. *J.Climate*, **13**, 3893–3914.

Dymnikov, V. P., 1988: Relationship of natural orthogonal components of the fields of meteorological characteristics to the eigenfunctions of dynamical operators. *Izv.Atmos.Oceanic Phys.*, **24**, 493–496.

Feldstein, S. B., 2002: Fundamental mechanisms of the growth and decay of the PNA teleconnection pattern. *Quart.J.R.Met.Soc.*, **128**, 775–796.

Fyfe, J. C., G. J. Boer, and G. M. Flato, 1999: The Arctic and Antarctic Oscillations and their projected changes under global warming. *Geophys.Res.Lett.*, **26**, 1601–1604.

Goodman, J., and J. Marshall, 2003: Using neutral singular vectors to study low–frequency atmospheric variability. *J.Climate*, in press.

Hoerling, M. P., J. W. Hurrell, and T. Xu, 2001: Tropical origins for recent North Atlantic climate change. *Science*, **292**, 90–92.

Honda, M., and H. Nakamura, 2001: Interannual seesaw between Aleutian and Icelandic lows. Part I: Seasonal dependence and life cycle. *J.Climate*, **14**, 1029–1042.

Hoskins, B. J., and T. Ambrizzi, 1993: Rossby wave propagation on a realistic longitudinally varying flow. *J.Atmos.Sci.*, **50**, 1661–1671.

Hoskins, B. J., and D. J. Karoly, 1981: The steady linear response of a spherical atmosphere to thermal and orographical forcing. *J.Atmos.Sci.*, **38**, 1179–1196.

Hurrell, J. W., 1995: Decadal trends in the North Atlantic oscillation: Regional temperatures and precipitation. *Science*, **269**, 676–679.

Hurrell, J. W., and H. van Loon, 1997: Decadal variations in climate associated with the North Atlantic Oscillation. *Clim.Change*, **36**, 301–326.

Itoh, H., 2002: True versus apparent Arctic Oscillation. *Geophys.Res.Lett.*, **29**, 10.1029/2001GL013978.

Itoh, H., and M. Kimoto, 1999: Weather regimes, low–frequency oscillations, and principal patterns of variability: A perspective of extratropical low–frequency variability. *J.Atmos.Sci.*, **56**, 2684–2705.

Jin, F.-F., M. Watanabe, L.-L. Pan, and J. Zhao, 2003a: Dynamics of synoptic eddy and low–frequency flow (SELF) feedback. Part I: A conceptual framework. *J.Atmos.Sci.*, submitted.

Jin, F.-F., L.-L. Pan, and M. Watanabe, 2003b: Dynamics of synoptic eddy and low–frequency flow (SELF) feedback. Part II: A barotropic theory for low–frequency modes. *J.Atmos.Sci.*, submitted.

Kalnay, E., and Co–authors, 1996: The NCEP/NCAR 40–year reanalysis project. *Bull.Amer.Meteor.Soc.*, **77**, 437–471.

Kimoto, M., and M. Ghil, 1993: Multiple flow regimes in the Northern Hemisphere winter. Part I: Methodology and hemispheric regimes. *J.Atmos.Sci.*, **50**, 2625–2643.

Kimoto, M., F.-F. Jin, M. Watanabe, and N. Yasutomi, 2001: Zonal–eddy coupling and a neutral mode theory for the Arctic Oscillation. *Geophys.Res.Lett.*, **28**, 737–740.

Kodera, K., and Y. Kuroda, 1999: Role of planetary waves in the stratosphere–troposphere coupled variability in the Northern Hemisphere winter. *Geophys.Res.Lett.*, **26**, 2375–2378.

Limpasuvan, V., and D. L. Hartmann, 1999: Eddies and the annular modes of climate variability. *Geophys.Res.Lett.*, **26**, 3133–3136.

Lorenz, E. N., 1963: Deterministic nonperiodic flow. *J.Atmos.Sci.*, **20**, 130–141.

Marshall, J., and F. Molteni, 1993: Toward a dynamical understanding of planetary–scale flow regimes. *J.Atmos.Sci.*, **50**, 1792–1818.

Metz, W., 1994: Singular modes and low–frequency atmospheric variability. *J.Atmos.Sci.*, **51**, 1740–1753.

Monahan, A. H., L. Pandolfo, and J. C. Fyfe, 2001: The preferred structure of variability of the Northern Hemisphere atmospheric circulation. *Geophys.Res.Lett.*, **28**, 1019–1022.

Navarra, A., 1993: A new set of orthonormal modes for linearized meteorological problems. *J.Atmos.Sci.*, **50**, 2569–2583.

Palmer, T. N., 1993: A nonlinear dynamical perspective on climate change. *Weather*, **48**, 314–326.

Peterson, K. A., R. J. Greatbatch, and J. Lu, 2002: Hindcasting the NAO using diabatic forcing of a simple AGCM. *Geophys.Res.Lett.*, **29**, 10.1029/2001GL014502.

Shindell, D. T., R. L. Miller, G. Schmidt, and L. Pandolfo, 1999: Simulation of recent northern winter climate trends by greenhouse–gas forcing. *Nature*, **399**, 452–455.

Simmons, A. J., J. M. Wallace, and G. Branstator, 1983: Barotropic wave propagation and instability, and atmospheric teleconnection patterns. *J.Atmos.Sci.*, **40**, 1363–1392.

Thompson, D. W. J., and J. M. Wallace, 1998: The Arctic Oscillation signature in the wintertime geopotential height and temperature fields. *Geophys.Res.Lett.*, **25**, 1297–1300.

Thompson, D. W. J., and J. M. Wallace, 2000: Annular modes in the extratropical circulation. Part I: Month–to–month variability. *J.Climate*, **13**, 1000–1016.

Thompson, D. W. J., and J. M. Wallace, 2001: Regional climate impacts of the Northern Hemisphere annular mode. *Science*, **293**, 85–89.

Ting, M., and I. M. Held, 1990: The stationary wave response to a tropical SST anomaly in an idealized GCM. *J.Atmos.Sci.*, **47**, 2546–2566.

Wallace, J. M., and D. S. Gutzler, 1981: Teleconnections in the geopotential height field during the Northern Hemisphere winter. *Mon.Wea.Rev.*, **109**, 784–812.

Wallace, J. M., Y. Zhang, and J. A. Renwick, 1995: Dynamic contribution to hemispheric mean temperature trends. *Science*, **270**, 780–783.

Wallace, J. M., 2000: North Atlantic Oscillation/annular mode: Two paradigms—one phenomenon. *Quart.J.R.Met.Soc.*, **126**, 791–805.

Wallace, J. M., and D. W. J. Thompson, 2002: The Pacific center of action of the Northern Hemisphere annular mode: Real or artifact? *J.Climate*, **15**, 1987–1991.

Watanabe, M., and T. Nitta, 1998: Relative impacts of snow and sea surface temperature anomalies on an extreme phase in the winter atmospheric circulation. *J.Climate*, **11**, 2837–2857.

Watanabe, M., and M. Kimoto, 2000: Atmosphere–ocean thermal coupling in the North Atlantic: A positive feedback. *Quart.J.R.Met.Soc.*, **126**, 3343–3369.; Corrigendum. **127**, 733–734.

Watanabe, M., 2003: Asian jet waveguide and a downstream extension of the North Atlantic Oscillation. *J.Climate*, submitted.

Figure captions

Fig.1 (a) Observed geopotential height anomaly at 300 hPa regressed on the winter (December–February) AO index. The values correspond to one standard deviation of the AO and the contour interval is 10 m, with the negative contours dashed. (b) As in (a) but for the zonal–mean zonal wind and E–P fluxes associated with anomalous stationary eddies. The contour interval is 0.5 m s^{-1}.

Fig.2 Inverse of singular values for $\boldsymbol{L}$. The first 50 modes are only shown.

Fig.3 (a) Geopotential height anomaly at $\sigma = 0.35$ for the v–vector with the smallest singular value (neutral mode, $\boldsymbol{v}_1$). (b) Zonal–mean zonal wind and E–P fluxes associated with the neutral mode. The contour intervals are the same as Fig. 1.

Fig.4 (a) As in Fig. 1a but for observed temperature anomaly at 925 hPa. The contour interval is 0.5 K and the negative contours are dashed. (b) As in Fig. 3a but for the temperature anomaly at $\sigma = 0.90$.

Fig.5 Observed winter anomalies in (a) 500 hPa geopotential height and (b) 925 hPa temperature, regressed on the winter PNA index. The contour interval is 10 m and 0.4 K, with the negative contours dotted. (c)–(d) As in (a)–(b) but for the height anomaly at $\sigma = 0.50$ and temperature anomaly at $\sigma = 0.95$ associated with the second v–vector.

Fig.6 As in Fig. 3a but for the third v–vector.

Fig.7 (a) Eddy components of the height anomalies (a) for the neutral mode and (b) diagnosed with a planetary wave model forced by $\boldsymbol{v}_1$. (c) Zonally averaged momentum fluxes ($\overline{u_a^* v_c^* + u_a^* v_a^*}$) at $\sigma = 0.20$ associated with the respective stationary eddy anomalies. (d) and (e) As in (b) but for the height responses induced by $\overline{\boldsymbol{v}}_1$ and $\boldsymbol{v}_1^*$, respectively. (f) As in (c) but for momentum fluxes associated with the eddy anomalies shown in (d) and (e).

Fig.8 (a) Zonally averaged momentum fluxes at 300 hPa associated with the AO stationary eddy anomalies (solid curve) and the neutral mode obtained by Kimoto et al. (2001) (dashed curve). (b) As in (a) but for momentum fluxes at $\sigma = 0.35$ associated with the

neutral mode obtained in this study (solid) and steady height response shown in Fig. 6d (dashed).

Fig.9 (a)–(d) Time evolution of the geopotential height (shading) and meridional wind (contour) anomalies at $\sigma = 0.35$ obtained in the LBM with $\boldsymbol{v}_1$ as the initial perturbation, which is confined to the Atlantic hemisphere (110°W–70°E). Each panel shows the daily average and the contour interval is 0.5 m s^{-1}. The gray lines in (d) indicate contours of the basic state zonal wind (30, 40, and 50 m s^{-1}). (e)–(h) As in (a)–(d) but with the initial $\boldsymbol{v}_1$ perturbation confined to the Pacific hemisphere (70°E–110°W). (i) As in (a) but for the observed AO anomalies. Note that the decay components have been removed in (a)–(h).

Fig.10 As in Fig. 7b but for the height responses induced by (a) $\boldsymbol{v}_1^{\rm bt}$ and (b) $\boldsymbol{v}_1^{\rm bc}$, respectively. See text for the definition of $\boldsymbol{v}_1^{\rm bt}$ and $\boldsymbol{v}_1^{\rm bc}$.

Fig.11 (a) Vertical profiles of linear damping coefficients in s^{-1}. Corresponding damping timescales are shown at the bottom. (b) Inverse singular values for seven different Newtonian damping profiles.

Fig.12 Spatial correlation coefficients between $\sigma_{0.35}$ height anomalies of the observed AO and the neutral mode with various coefficients of the Rayleigh friction (γ) and Newtonian cooling (α). The contour interval is 0.1 and supplemental dashed contour (interval 0.01) is drawn for above 0.7. The star denotes a set of standard parameters.

Fig.13 Optimal forcing (u–vector) for temperature at (a) $\sigma = 0.81$ and (b) $\sigma = 0.35$ to the neutral mode. The contour interval is 0.03 K day^{-1} and the dark (light) shading indicates heating (cooling) greater than 0.03 K day^{-1} (less than -0.03 K day^{-1}).

Fig.14 (a) Steady height response at $\sigma = 0.35$ to the optimal thermal forcing. The contour interval is 10 m. (b) and (c) As in (a) but for the response to the tropical (20°S–20°N) and extratropical (20°N–90°N) thermal forcing, respectively.

Fig.A1 The Lorenz attractor, (a) 3D plot and (b) 2D projections. The gray lines denote the axis of three EOFs based on the time integration of the Lorenz model.

Fig.A2 As in Fig. A1 but for the lines denoting the axis of three singular vectors based on the model linearized operator.

Fig.A3 Inner products of the leading EOF and $\boldsymbol{v}_1$ (thin contour with shading) and the inverse singular value σ_1^{-1} (thick contour), superimposed on the Lorenz attractor projected onto a plane spanned by EOFs 1 and 2. The singular vector is computed with basic states varied on the EOF plane. The thick contour denotes an isoline of $\sigma_1^{-1} = 1$ and a narrow area between the two isolines indicates the greater singularity.

Fig.A4 (a)–(c) 2D projection of the unforced Lorenz model. (d)–(f) As in (a)–(c) but for the steady forcing vector parallel to $\boldsymbol{u}_1$, (-5.4, 19.3, 0.0), included. The thick arrows indicate the direction of $\boldsymbol{v}_1$ excited by $\boldsymbol{u}_1$.

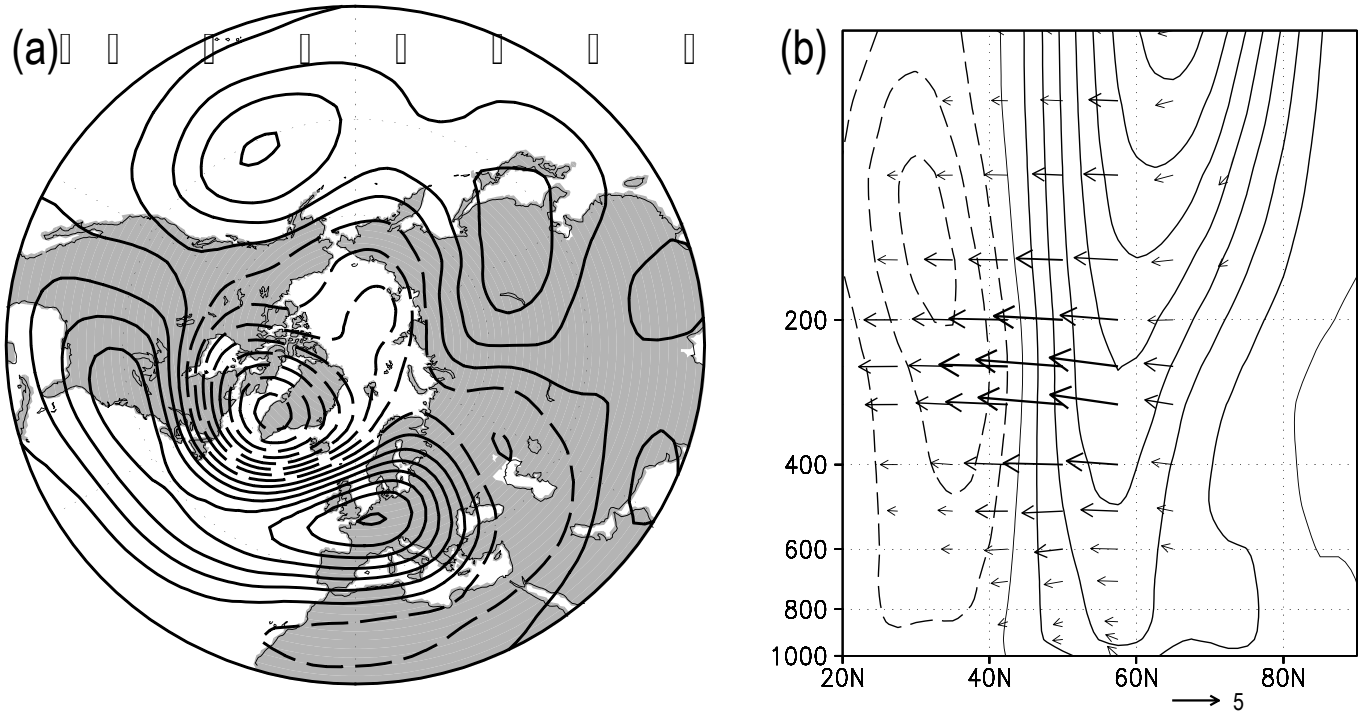

Figure 1.

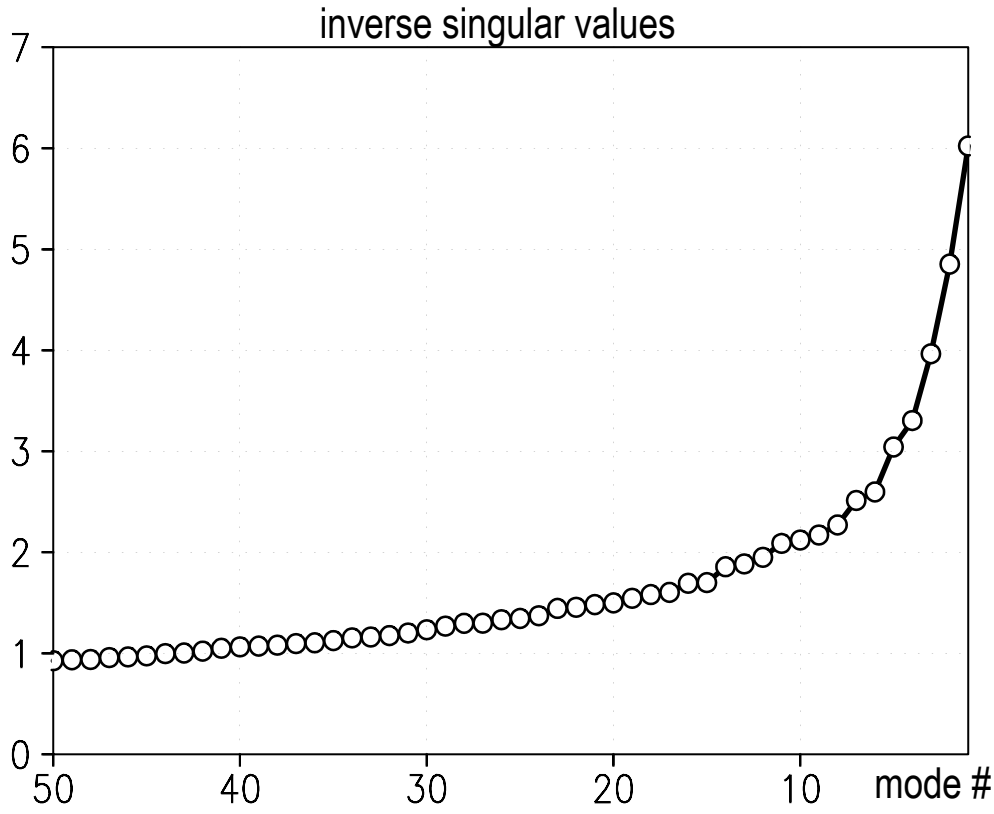

Figure 2.

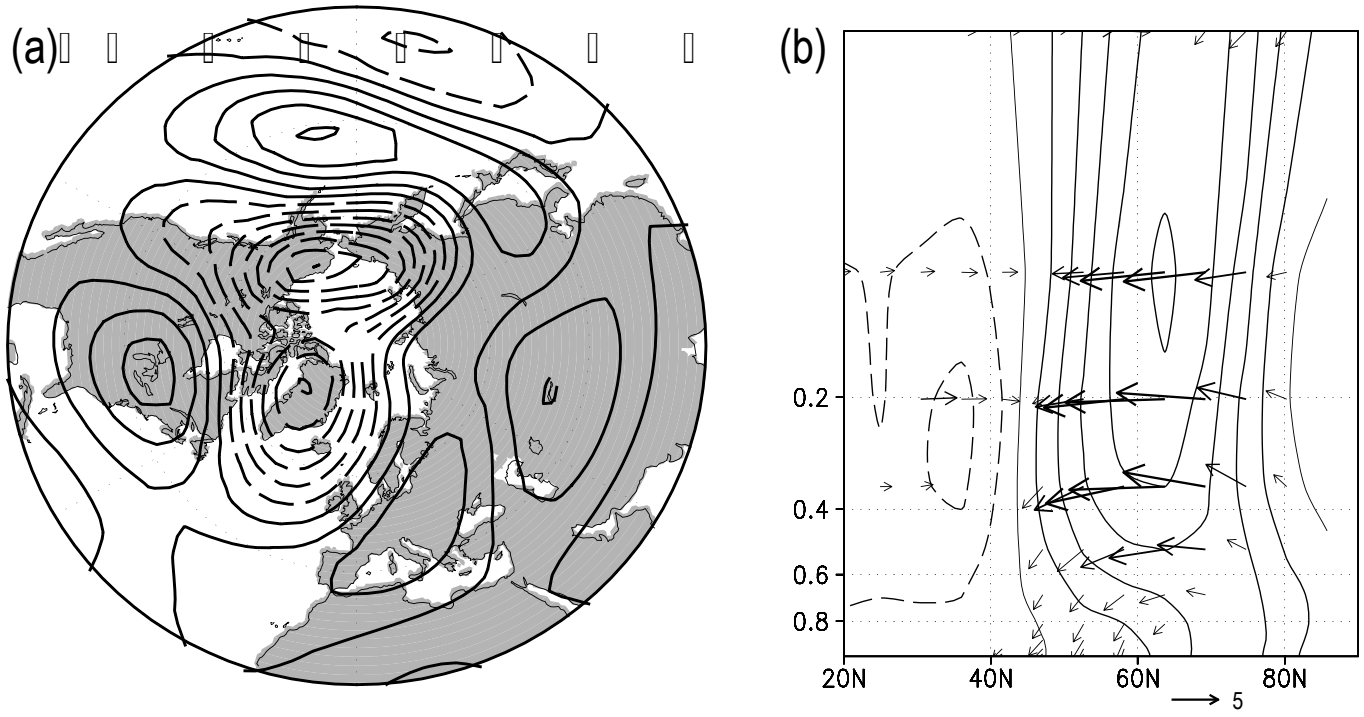

Figure 3.

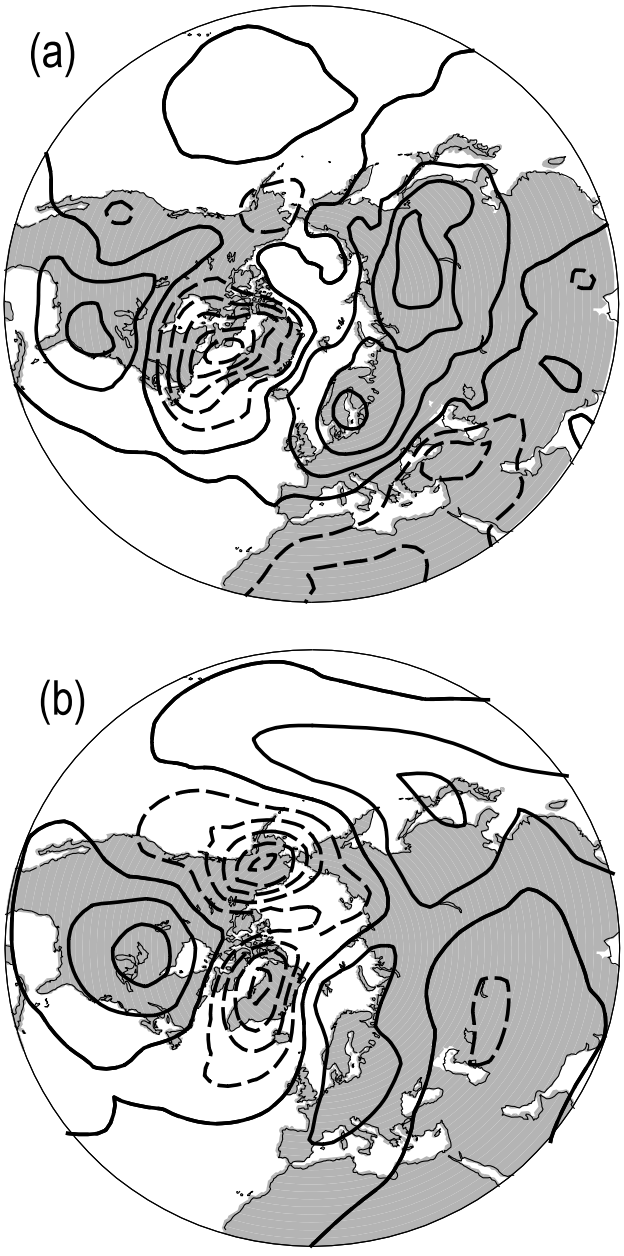

Figure 4.

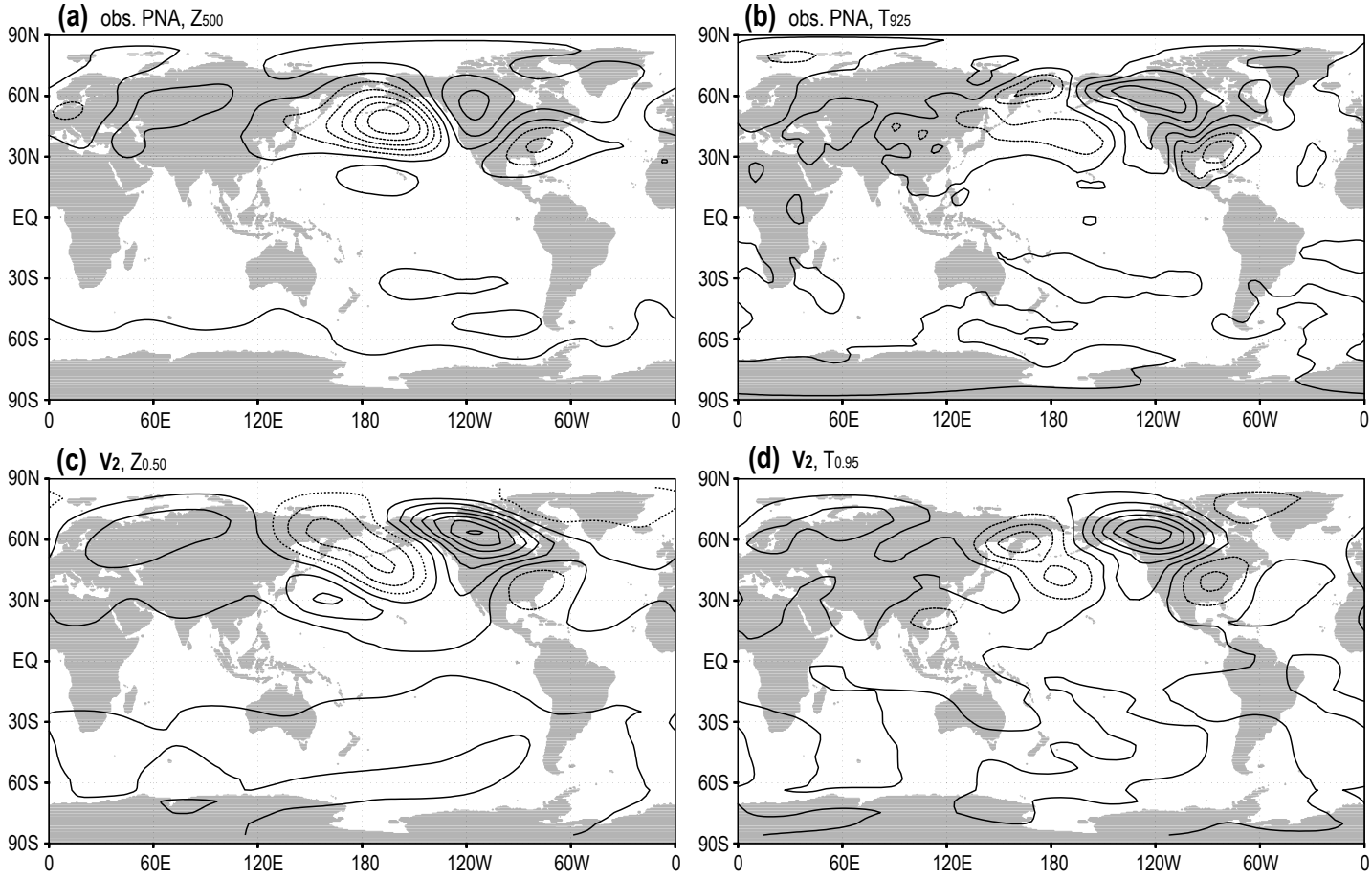
(a) obs. PNA, Z500
(b) obs. PNA, T925
(c) V2, Z0.50
(d) V2, T0.95
90N
60N
30N
EQ
30S
60S
90S
0
60E
120E
180
120W
60W
0

Figure 5.

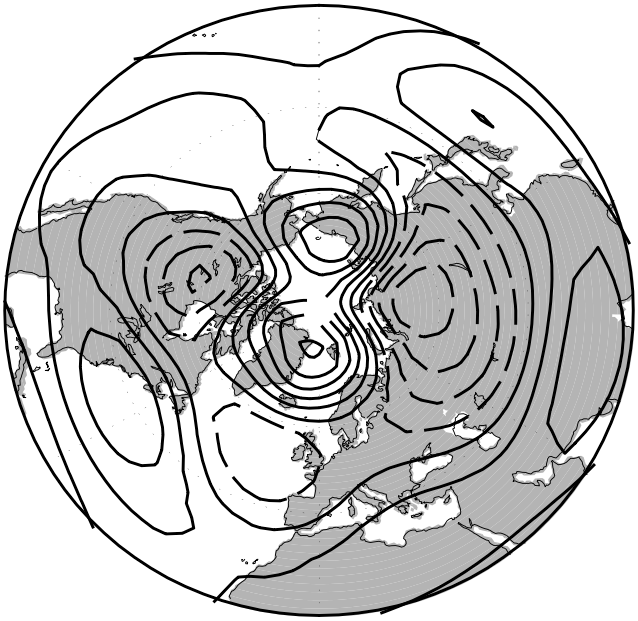

Figure 6.

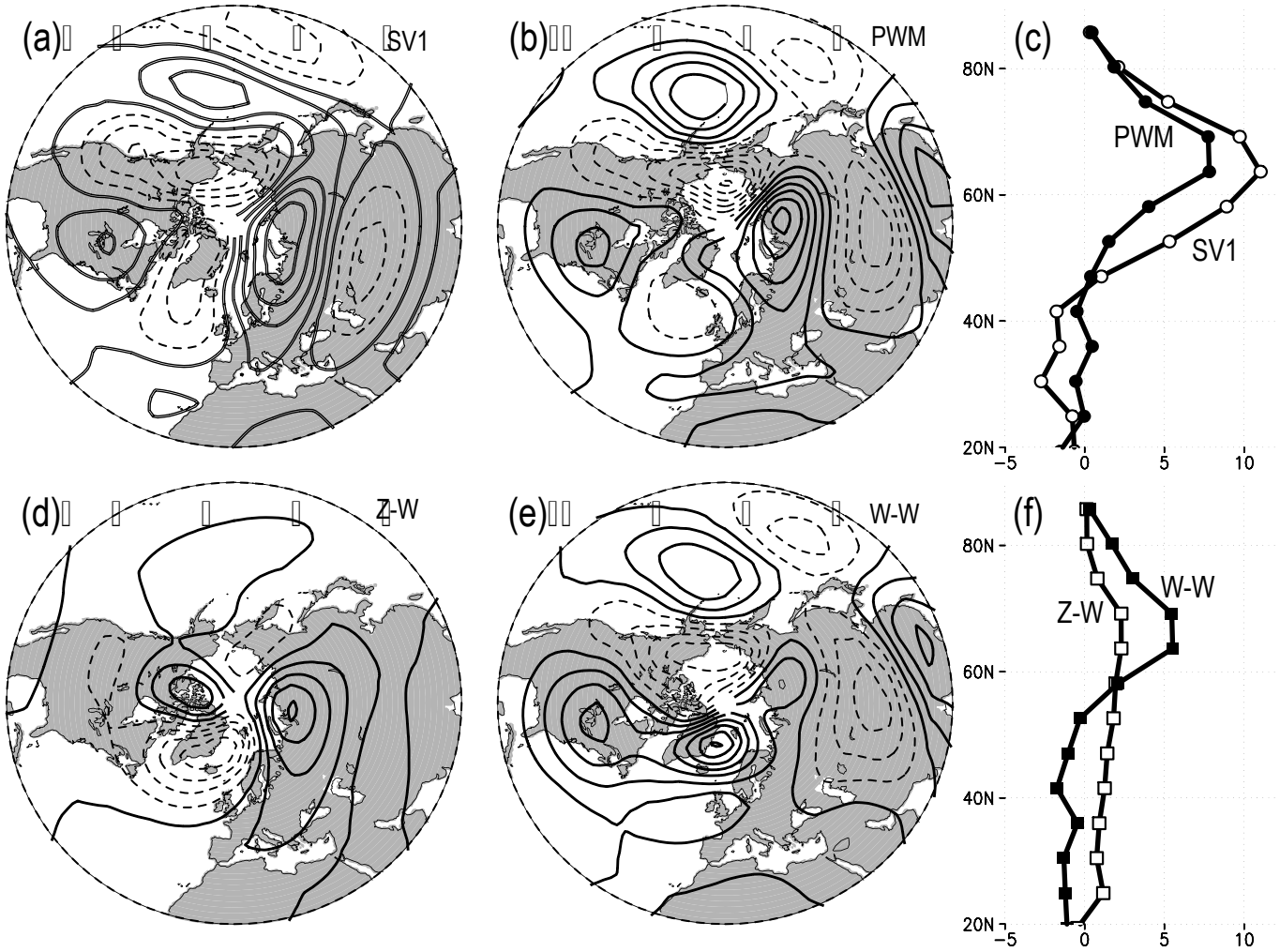
(a)
SV1
(b)
PWM
(c)
80N
60N
40N
20N
PWM
SV1
−5
0
5
10
(d)
Z-W
(e)
W-W
(f)
80N
60N
40N
20N
W-W
Z-W
−5
0
5
10

Figure 7.

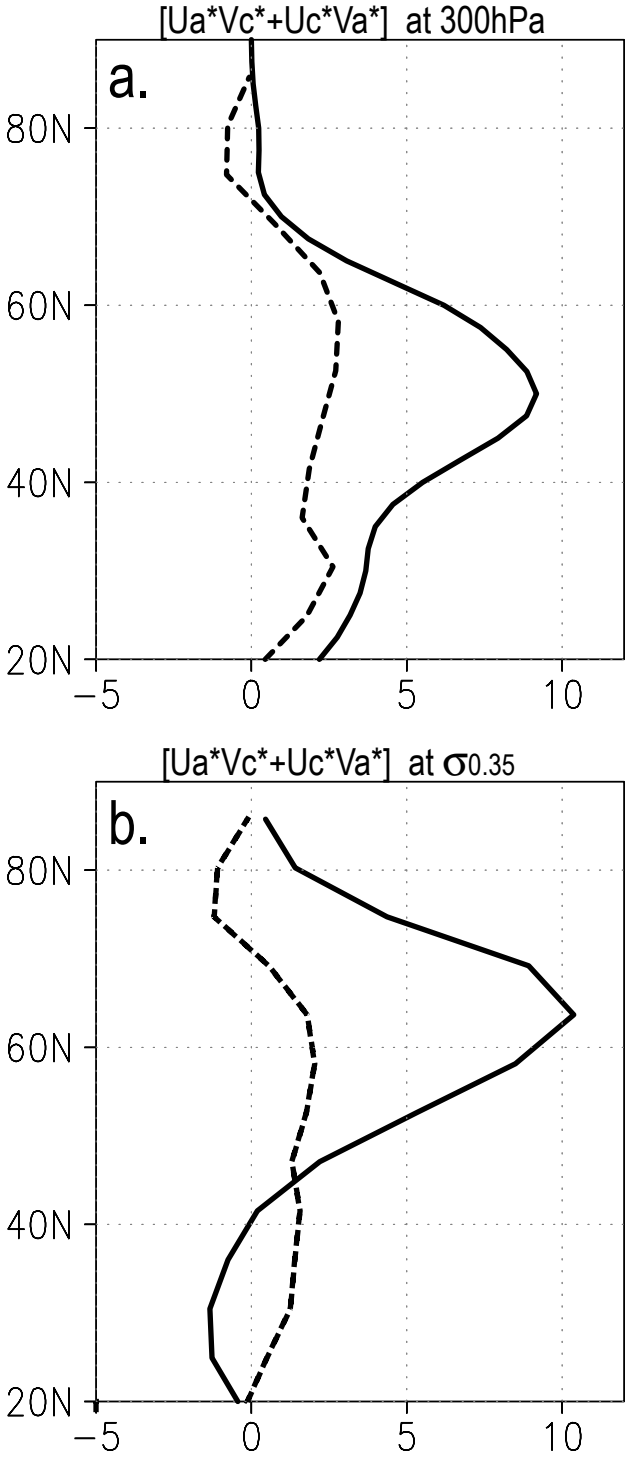
[Ua*Vc*+Uc*Va*] at 300hPa
a.
80N
60N
40N
20N
−5
0
5
10
[Ua*Vc*+Uc*Va*] at σ0.35
b.
80N
60N
40N
20N
−5
0
5
10

Figure 8.

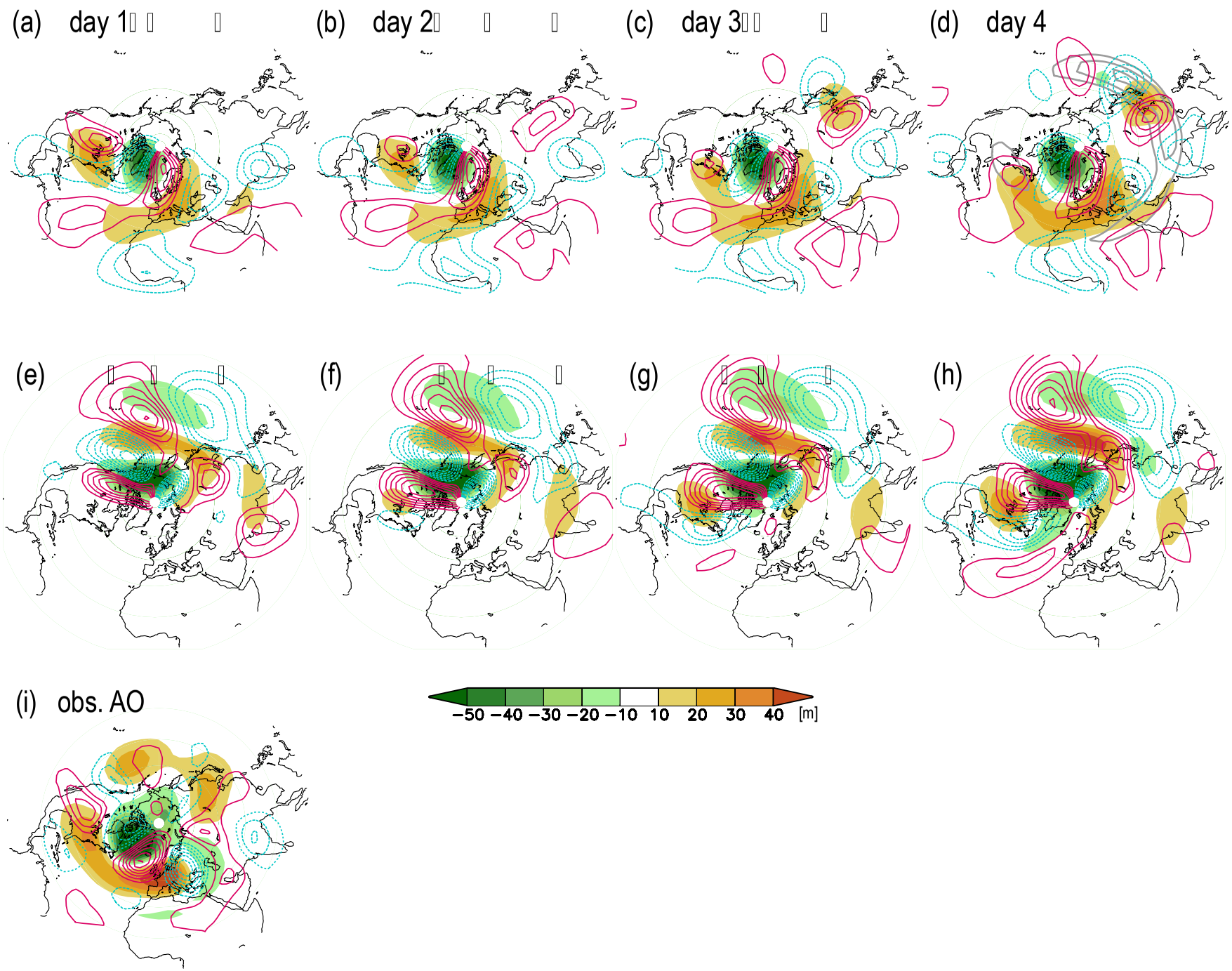

Figure 9.

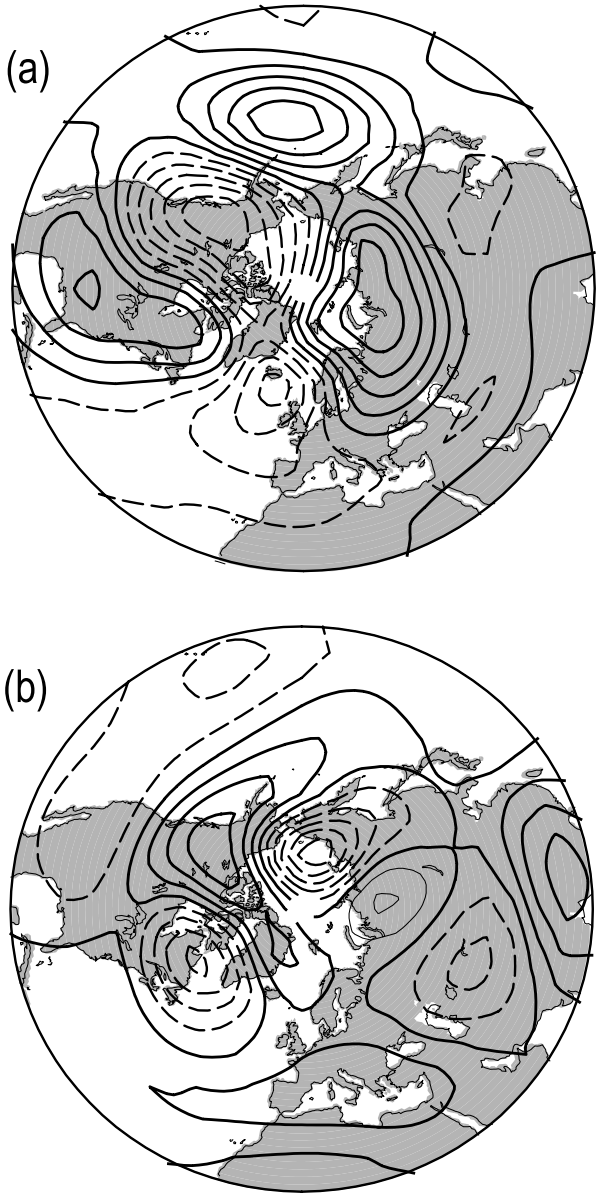

Figure 10.

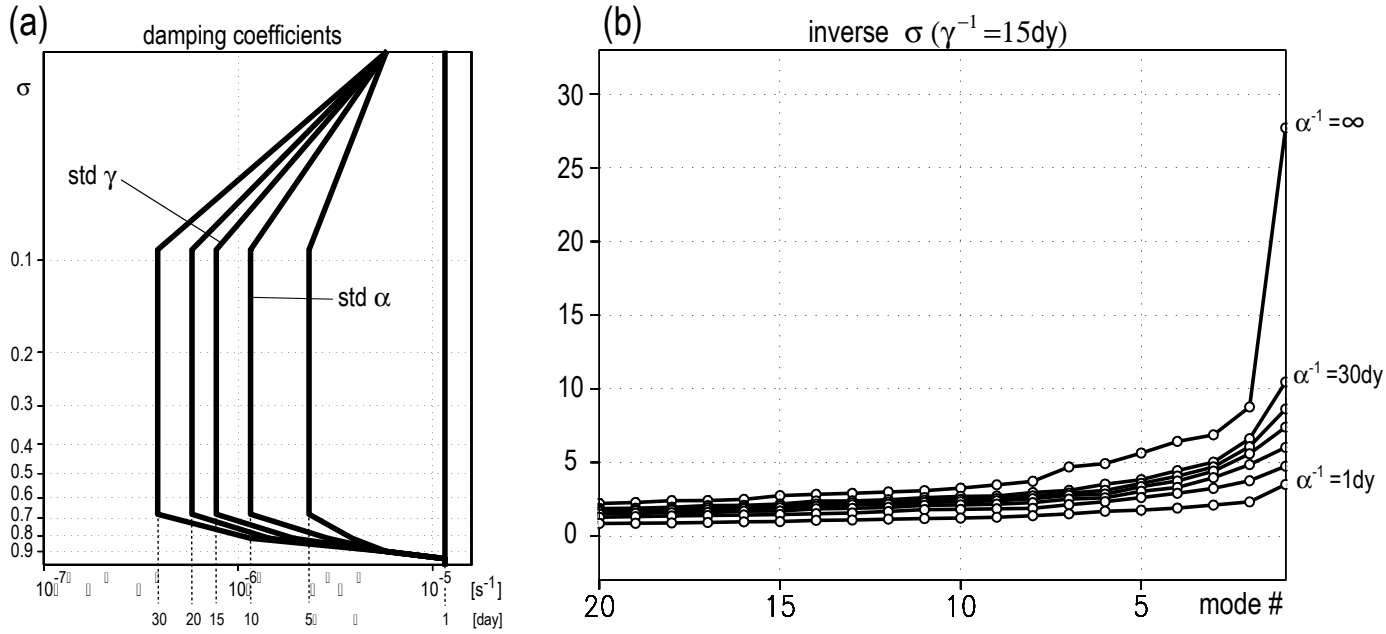
(a)
damping coefficients
σ
std γ
std α
0.1
0.2
0.3
0.4
0.5
0.6
0.7
0.8
0.9
10^-7
10^-6
10^-5
[s^-1]
30 20 15 10 5 1 [day]
(b)
inverse σ (γ^-1 =15dy)
30
25
20
15
10
5
0
α^-1 =∞
α^-1 =30dy
α^-1 =1dy
20 15 10 5 mode #

Figure 11.

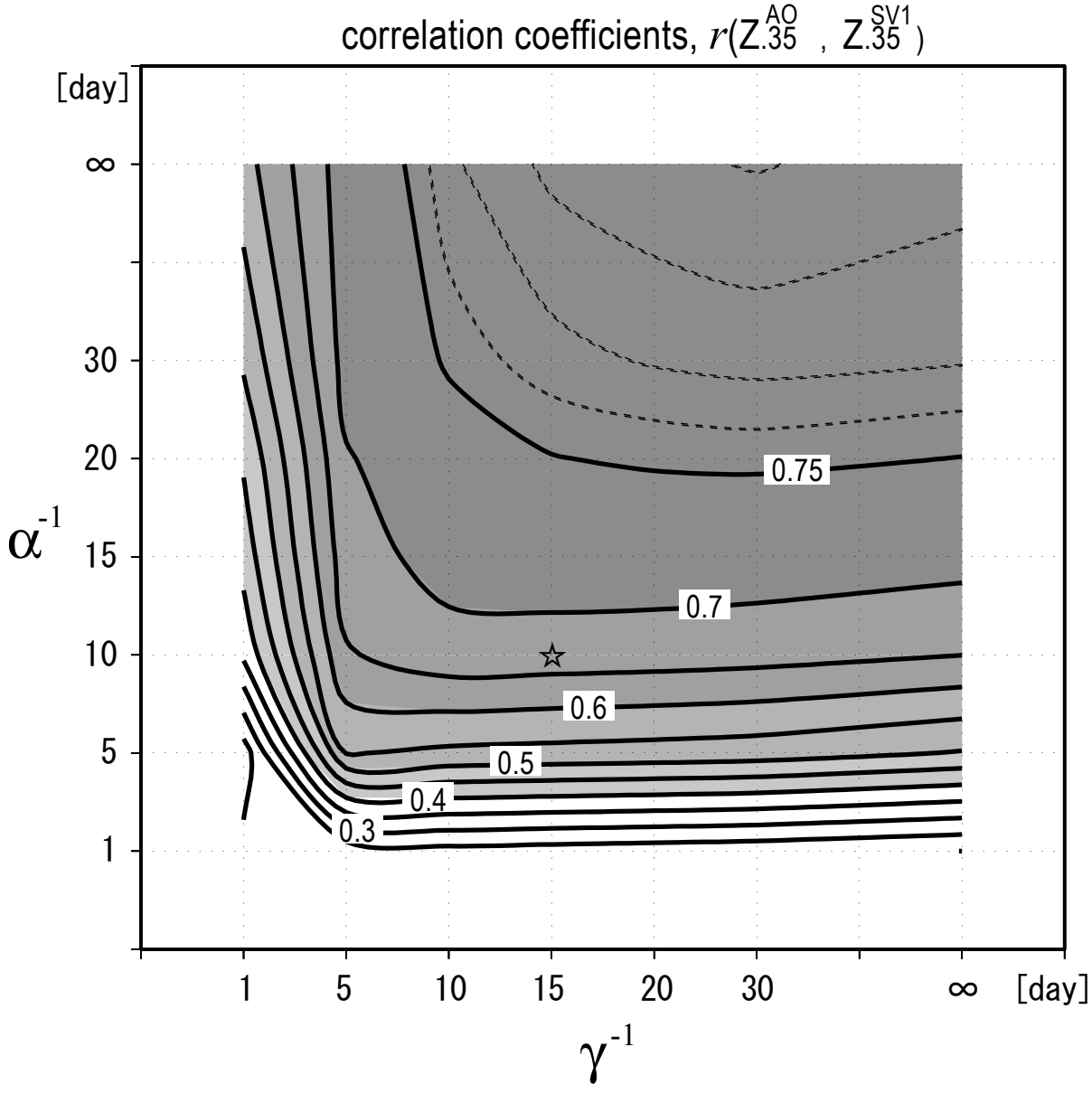
correlation coefficients, $r(Z_{.35}^{AO}, Z_{.35}^{SV1})$
[day]
∞
30
20
15
10
5
1
α^{-1}
0.75
0.7
0.6
0.5
0.4
0.3
1
5
10
15
20
30
∞
[day]
γ^{-1}

Figure 12.

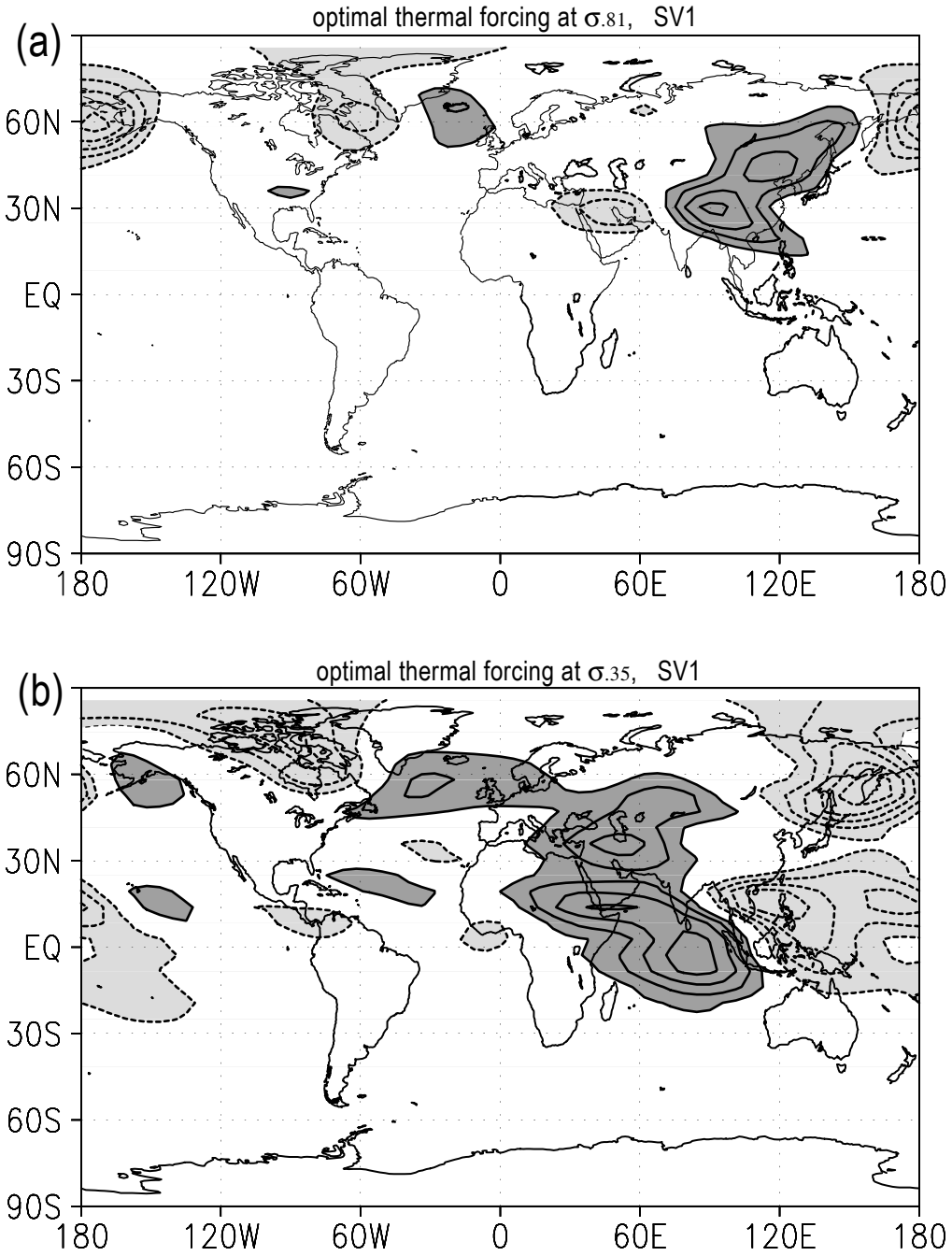
(a)
optimal thermal forcing at σ.81, SV1
60N
30N
EQ
30S
60S
90S
180
120W
60W
0
60E
120E
180
(b)
optimal thermal forcing at σ.35, SV1
60N
30N
EQ
30S
60S
90S
180
120W
60W
0
60E
120E
180

Figure 13.

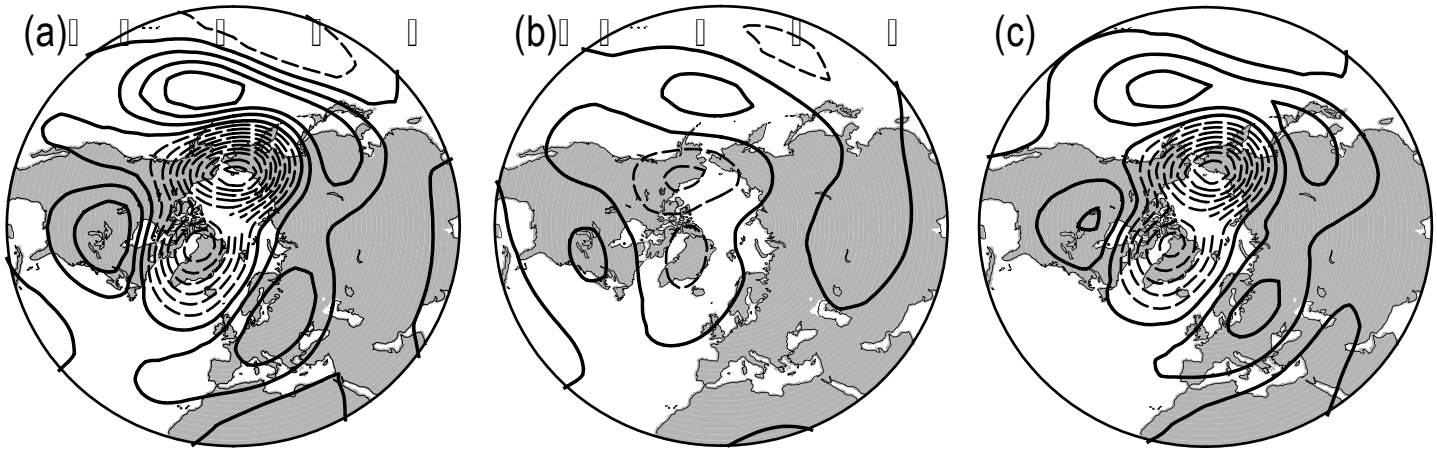

Figure 14.

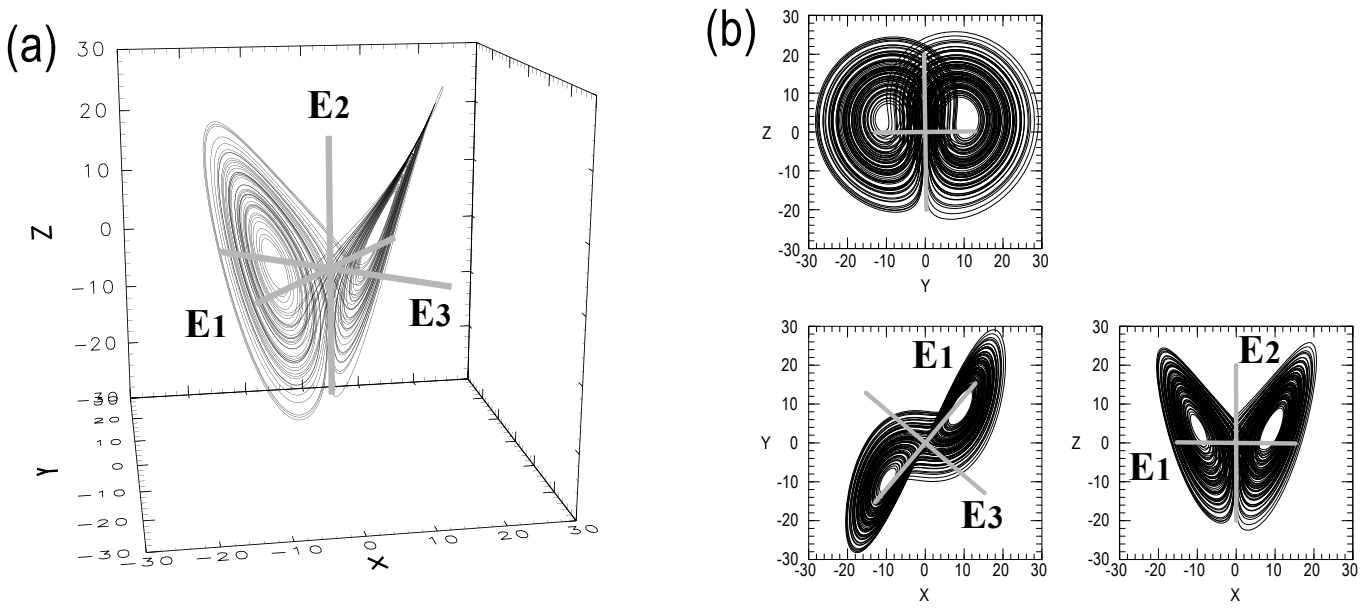

Figure A1.

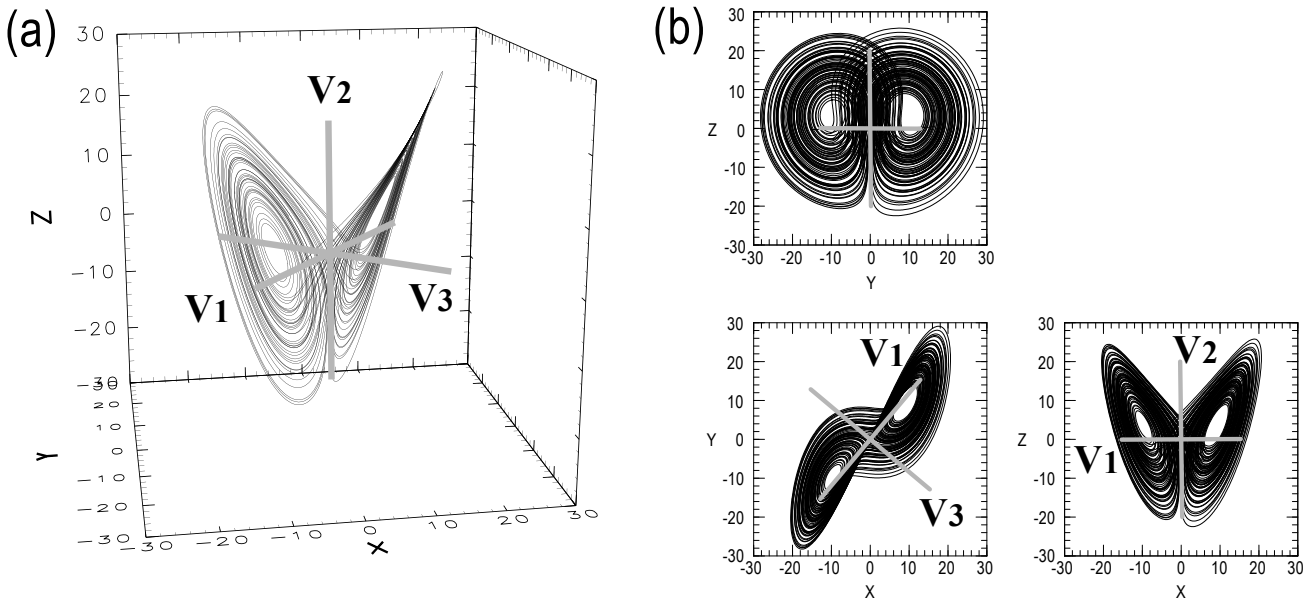

Figure A2.

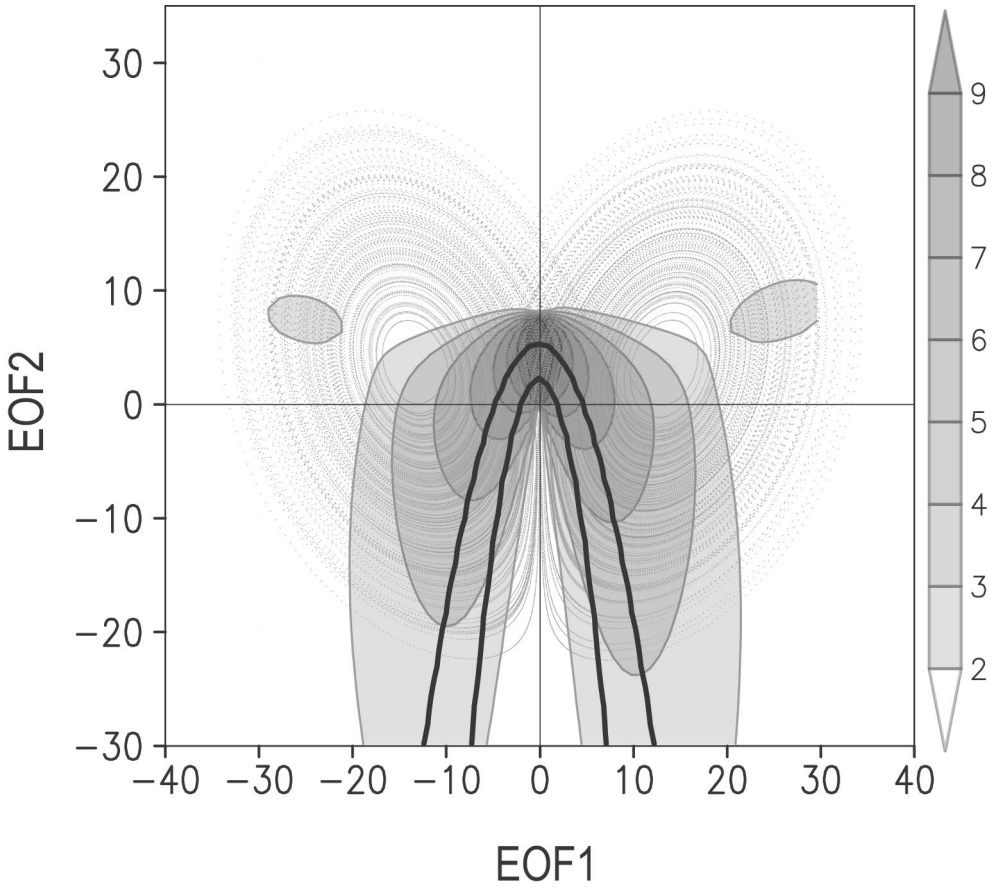

Figure A3.

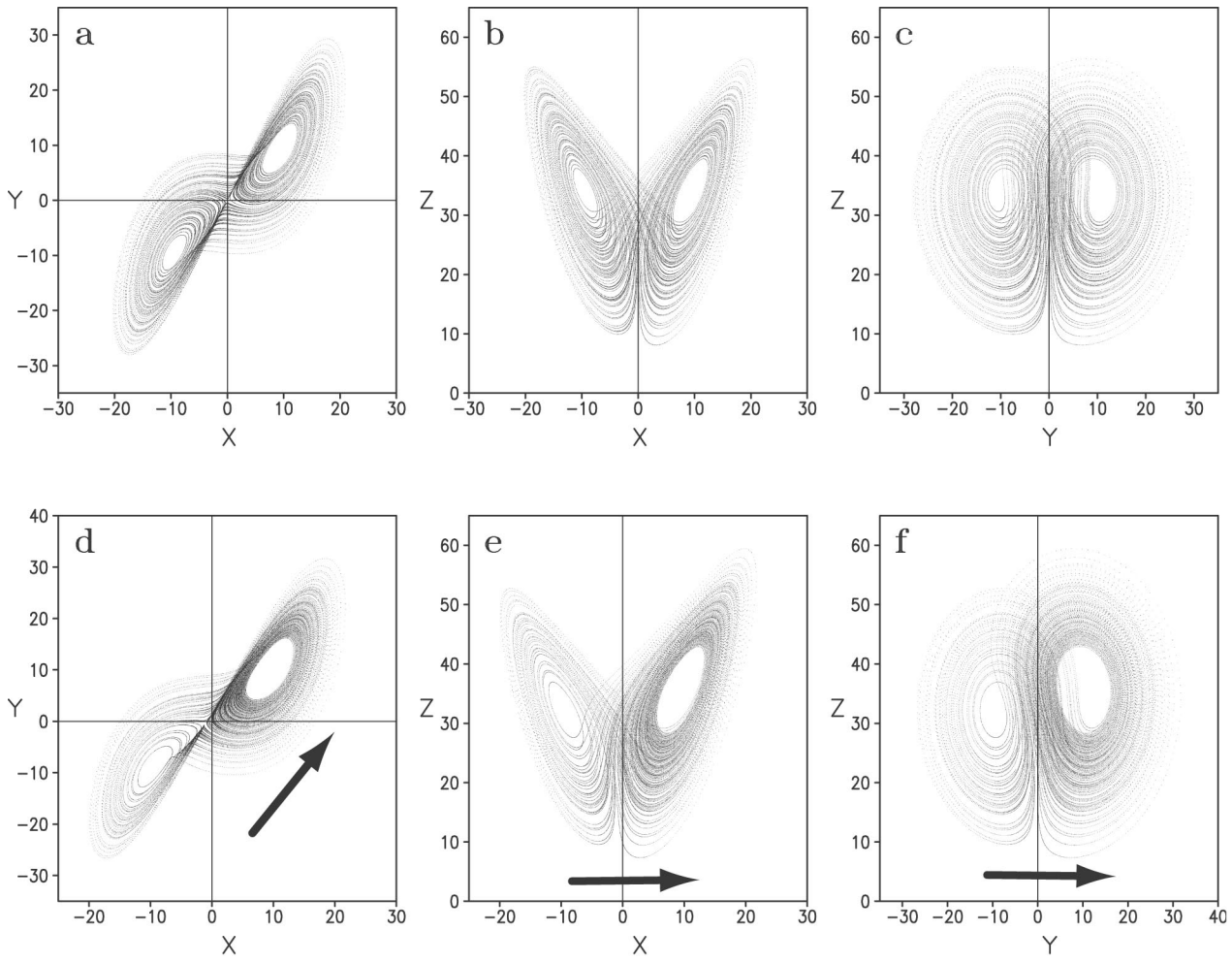

Figure A4.